fluids

MDPI

Article

Vortex-Induced Vibrations of a 2DOF Rigid Cylinder with Hard Marine Growth in Turbulent Oscillatory Flow

Henry Francis Annapeh and Victoria Kurushina *

Laboratory of Vibration and Hydrodynamics Modelling, Industrial University of Tyumen,
Tyumen 625000, Russia; annapeg@tyuiu.ru
* Correspondence: v.kurushina@outlook.com or kurushinava@tyuiu.ru

Abstract

This paper presents a numerical investigation into the vortex-induced vibrations (VIV) of a smooth and a marine-fouled circular cylinder with two degrees of freedom (2DOF), subjected to a turbulent oscillatory flow. The study aims to elucidate the critical influence of the Keulegan-Carpenter (*KC*) number of 5, 10, and 15 on the vibration response, lock-in regime, frequency synchronization, trajectory patterns and vorticity. Simulations are performed by solving the two-dimensional unsteady Reynolds-Averaged Navier–Stokes (RANS) equations with the Shear Stress Transport (SST) k-ω turbulence model in ANSYS Fluent 2025 R1. An increase in the *KC* number leads to a significant broadening of the lock-in region, an increase in maximum vibration amplitudes and their emergence at higher reduced velocities. Another key finding is the consistent suppressive effect of biofouling on cross-flow vibrations. The biofouled cylinder exhibits lower cross-flow amplitudes across all *KC* numbers compared to the smooth cylinder, almost plateauing at around 1.0D for KC = 10 and 15, while the smooth cylinder reaches amplitudes of up to 1.8D and a maximum in-line amplitude of 4.46D. These findings have critical implications for the realistic fatigue life assessment and design of offshore marine structures, highlighting the necessity of incorporating surface roughness effects into VIV prediction models.

Keywords: vortex-induced vibration; biofouling; oscillatory flow; lock-in; two-degrees-of-freedom structure

Check for updates

Academic Editors: Luiz Antonio Alcântara Pereira and Alex Mendonça Bimbato

Received: 26 December 2025
Revised: 13 February 2026
Accepted: 16 February 2026
Published: 18 February 2026

1. Introduction

Slender offshore structures, such as risers, cables and supports, are subject to the hard and soft marine growth [1], developing during regular operations of energy production systems. Specific impacts on the weight of the structure and dynamic response due to waves and currents depend on exact species settling on subsea objects, as discussed in [2]. According to [3], marine growth depends on the water depth significantly, varying from mussels in proximity to the sea surface to hydroids, widely spread at depths below 110 m. However, hard biofouling largely presented by barnacles remains a dominant problem [4] for subsea structures at different depths, affecting the long-term functionality.

Vortex-induced vibration (VIV) of slender subsea structures is a known challenge to their performance [5], characterized by displacement amplitudes, fluctuations of lift and drag forces, vortex street type and vortex shedding frequency. The peak impact of VIVs is observed during the lock-in of the vibration frequency at the level of the natural frequency of the structure, linked to the proximity of the vortex shedding frequency and the natural frequency. This phenomenon is discussed in comprehensive reviews by [6–8] and is

https://doi.org/10.3390/fluids11020055

related to observations of increased displacement and fluid force amplitudes, compromising the safety of offshore operations. The lock-in condition poses a significant problem for the design of offshore structures due to its sensitivity to multiple factors including, but not limited to the expected flow type and velocity, mass, damping and aspect ratios of the structure, surface roughness. The general recommendation from the VIV analysis, according to [9], is to design structures before or after the lock-in region in the predicted flow velocity range. Hard marine growth, altering the shape and dimensions of a structure, adds more unpredictability in identifying conditions when a lock-in could be expected, and this phenomenon requires new detailed studies looking into the structural behavior in various flow types and with different biofouling scenarios.

A series of experimental studies on hard biofouling of slender structures in uniform flows begins with the investigation by [10] into the regular pyramidal roughness with Reynolds number ranging from 3500 to 35,000. It is found that the hard marine fouling reduces the majority of VIV characteristics, including the maximum displacement amplitude, the lock-in range, the lift force coefficient, the mean and fluctuating drag coefficients. It is also observed to reduce sizes of shed vortices and length of the recirculation zone behind the cylindrical object.

Following these observations, the experimental study by [11] considers Reynolds number range from 7800 to 49,000 and compares aggregated and regular hard marine fouling. In both cases, the study finds that maximum vibration amplitudes and lift coefficients are smaller than for a smooth structure. This work also reports that a suppression of VIV can be increased by reducing the biofouling coverage. Observations of [11] suggest that the most impactful factors defining the VIV development with biofouling are the coverage ratio and aggregation, while the flow incidence and the shape of a fouling element have a lesser effect.

The authors of [12] extend these findings to tandem cylinders covered with hard marine fouling, employing pyramid-like elements. The arrangement of smooth tandem cylinders is selected to demonstrate both VIV and galloping for the downstream structure. The distance between cylinders varies in this work from 3 to 7 diameters, while the upstream cylinder is assumed to be fixed. The marine fouling is observed to eliminate the galloping and reduce the VIV part of the response of the downstream cylinder, which is consistent with earlier studies for a single structure. The lift coefficient is shown to reduce by about 33% for a fouled structure, and the maximum displacement amplitude reduces to 35% of the amplitude developed by the smooth cylinder.

Following the consideration of tandem structures, the authors of [13] investigate effects of the surface roughness on the flow field and flow-induced vibration characteristics for an array of eight structures in uniform flow. In this work, the combined effect of the position of downstream structures and surface roughness is observed at lower flow velocities, so that vibration amplitudes are lower for tubes with a roughness compared to smooth tubes. At the same time, at higher flow velocities, the study reports increased displacement amplitudes of the tube bundle overall.

Approximately at the same time, the hard marine growth for a submarine cable is evaluated in the experimental work by [14]. This research examines seven roughness configurations and three flow conditions, including current-only, wave-only and combined wave and current. The study reviews the homogeneous and non-homogeneous roughness and identifies lower drag coefficients for the non-homogeneous cases. Similar flow conditions are considered in the experiments by [15], involving varying the height and coverage ratio of biofouling elements. In this work, the drag coefficient increases with the growing roughness height and coverage ratio for the current-only conditions, while it is significantly less affected in the case of wave-only load. At the same time, the combined current and wave conditions lead to effects similar to the current-only case.

Advancing understanding of the hard marine growth, dynamics a two degrees-of-freedom (2DOF) structure, experiencing VIV, is evaluated by [16] in the series of towing tank experiments. The Reynolds number varies in this research from 6400 to 52,000. As a result of biofouling, the maximum displacement amplitude is reduced by 37% in the in-line direction, and by 50% in the cross-flow direction. The hard marine fouling is found to reduce the maximum lift coefficient and to significantly decrease the maximum drag coefficient. The lock-in range is observed to also reduce in width in the reduced velocity range, together with the reduction in the lower branch length, and the beginning of the lower branch occurs earlier in the reduced velocity range. These effects manifest at 33% coverage ratio of the fouling, and they are less pronounced when the coverage ratio increases.

Negative effects of hard marine growth on energy harvesting devices are evaluated in experimental studies by [17,18]. In [17], a hard marine growth reduces the energy transfer ratio by 15–36% for a single rigid cylinder harvesting energy from VIV. The marine fouling irregularity also is observed in this work to be less significant for the VIV response, compared to the impact of the coverage ratio. The research by [18] compares energy harvesting oscillators with one and two degrees of freedom for Reynolds number range from 6400 to 52,000. The performance of 2DOF oscillators is found to decrease by 75%, compared to the clean oscillator, while results for 1DOF oscillators are consistent with previous findings.

In summary, these works provide a strong foundation for understanding the impacts of hard biofouling on the dynamics of slender structures, however, the present state of the art is limited to uniform steady flows and some types of waves, and the consideration of 2DOF structures is still rare. This makes investigations into dynamic and complex flows for 2DOF rigid objects a promising yet unexplored research direction.

Modeling attempts to predict dynamics of a slender structure with hard marine growth are also relatively limited. In [19], a finite element model is established in order to quantify effects of hard marine fouling on flow-induced vibrations of pipelines conveying fluid, with an application to heat exchangers. The paper considers a pulsating internal flow, different external flow velocities and fouling levels from 0% to 60%, and uses fluid-solid coupling. The study reports an increase in the wall load, structural displacement and acceleration with increasing biofouling and with a growing inlet flow velocity. Another modeling attempt is undertaken by [20], who propose a modeling approach for the dynamics of a slender structure subjected to an external uniform flow through modification of the Morison's equation to account for marine fouling effects. Studies for similar offshore structures subjected to marine growth include a modeling effort for a large-area flexible net by [21], considering three possible scenarios of marine growth in irregular waves.

A related branch of studies focuses on the dynamics of structures covered with soft organisms, and these investigations are very recent. Experiments with soft marine fouling are conducted by [2] for a one degree-of-freedom (1DOF) structure, oscillating transversally in a uniform flow of Reynolds number from 5500 to 55,000. Hydroid species are considered, and it is found that the vibration amplitude with a soft marine growth is 10% lower than with a hard marine growth. It is observed that displacement amplitudes and fluid force coefficients decrease by 30–40% with partial soft marine fouling, while a full coverage results in a further decrease by 8–17%.

Soft fouling with moss is studied by [22] with the coverage ratio from 0% to 60%. The widest lock-in region is experienced by the structure with the coverage ratio of 30%. The maximum cross-flow amplitude is lower with the moss overall than for a smooth structure, and is observed to occur later in the reduced velocity range. At the same time, the in-line response becomes more significant with the soft marine fouling. Also, the study observes changes from a 2S vortex shedding pattern to 2P and 2T pattern with the increase in the coverage ratio.

Similar to hard marine fouling, the study by [23] analyses impacts of a soft marine growth on energy harvesting based on VIV for a 1DOF oscillator working in the Reynolds number range from 5500 to 55,000. Soft biofouling is found to reduce the harnessed power by 59% and the energy transfer ratio by 62%. The subsequent study by [24] discusses energy harvesting based on VIV of a circular 2DOF structure with soft fouling. This work considers three coverage ratios of 33%, 67% and 100%, and it is found that the full coverage of a 2DOF oscillator reduces the performance by 60%.

Soft marine fouling is also studied in [25,26] for aquaculture cages in regular and irregular waves. In the latter study, effects of biofouling are found to be stronger in irregular waves, where the surge (in-line) force amplitude is observed to increase by 160%, while the sway (cross-flow) force reduces by 50%.

In addition to existing works on biofouling, the present research on VIV in oscillatory flows covers rigid [27,28] and flexible [29,30] structures, including when also subjected to the impact of internal flows [31,32]. Despite recent advances in experimental and modeling research of VIV in oscillatory flows, biofouled structures have not been considered in published studies yet.

The literature survey indicates a general lack of simulation attempts to look into the VIV dynamics of single structures with biofouling in various conditions. There is a visible lack of research into impacts of an oscillatory flow and other dynamic, nonuniform, complex flows on the development of the lock-in condition of 2DOF rigid structures with a hard or soft marine growth. The current study attempts to fill this gap by evaluating the lock-in characteristics of a slender 2DOF structure with a hard marine growth in a turbulent oscillatory flow with the 2D computational fluid dynamics approach, benchmarked with published experimental data for a fouled structure. The study attempts to observe an evolution of the lock-in state through three frequently encountered Keulegan–Carpenter (*KC*) numbers of 5, 10 and 15, and to identify differences with the dynamics of a smooth structure in the oscillatory flow.

The paper is organized in four sections. The Section 1 outlines major works in the present state of the art of research on hard and soft marine fouling of slender structures. The computational fluid dynamics model implemented in ANSYS Fluent 2025 R1 with verification and validation is presented in the Section 2. The Section 3 provides simulation results for the observed VIV lock-in condition in terms of displacement amplitudes, frequency spectra, structural trajectories and vorticity contours. The Section 4 concludes the research with the list of main findings.

2. Numerical Method

2.1. Problem Description

A 2DOF motion of a single smooth and fouled circular cylinder subjected to an oscillatory flow of different *KC* numbers in a turbulent flow regime in two dimensions (2D) is numerically investigated in the current work. The general schematic of the computational domain is shown in Figure 1a. *KC* numbers of 5, 10 and 15 are considered, and structural parameters are shown in Table 1, consistent with the experimental research [10]. The effect of *KC* numbers on response amplitudes, the lock-in regime, frequency ratios, trajectories and vorticity contours for the smooth and biofouled cylinders undergoing oscillations is examined. The in-line and cross-flow natural frequencies of cylinders are kept constant. Simulations are performed for Reynolds numbers ranging from 9251 to 92,505 for the

https://doi.org/10.3390/fluids11020055

considered *KC* numbers. The reduced velocity interval of 2–20 is chosen to observe the full lock-in regime of a 2DOF rigid structure. Within this flow regime, vortex-induced vibration is primarily governed by large-scale coherent vortex shedding, particularly in oscillatory flow where the flow reversal constrains the growth of strong spanwise instabilities. The structural response is therefore dominated by cross-sectional fluid–structure interaction mechanisms that can be reasonably approximated using a 2D vibration model. This approach is consistent with the objective of the present study, which focuses on the local wake dynamics, lock-in behavior, and comparative response trends between smooth and biofouled cylinders.

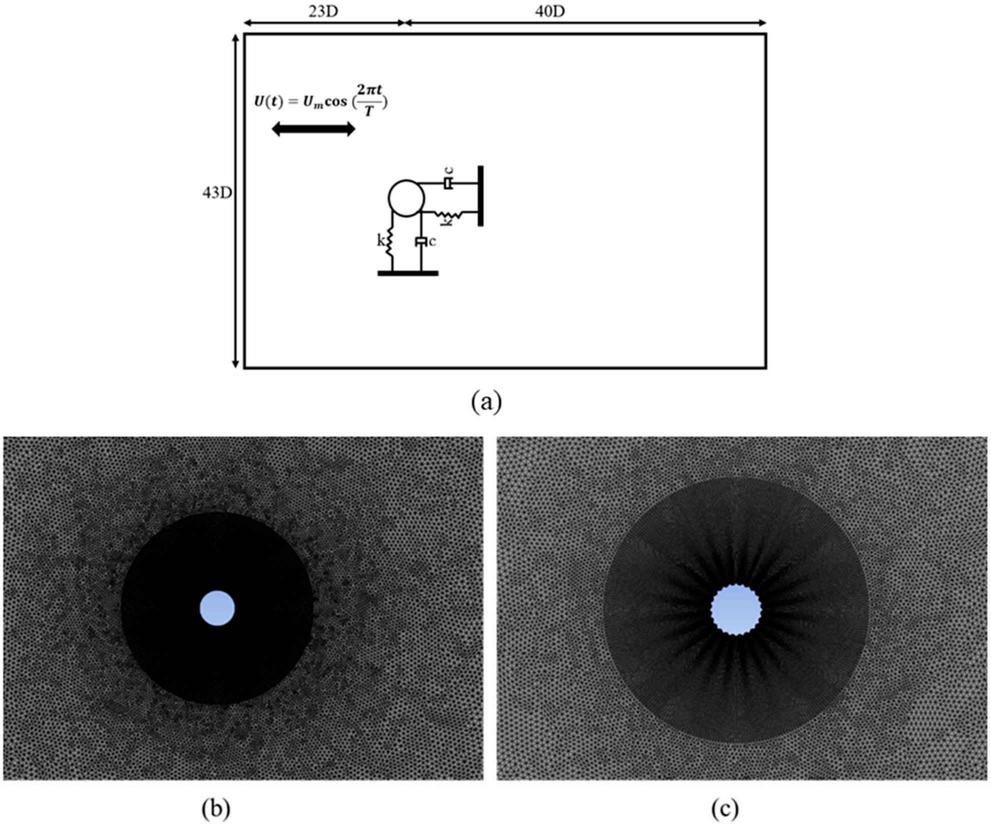

Figure 1. General schematic of the considered case: (**a**) schematic of the computational domain; (**b**) mesh around the smooth cylinder; (**c**) mesh around the biofouled cylinder.

Table 1. Structural parameters for main simulations in the current work.

Parameter, Symbol	Value and Units
Smooth cylinder diameter, D	0.065 m
Damping ratio, ζ	0.005
Mass ratio, m^*	4.8
Natural frequency, f_n	1.1 Hz
Triangle height, h	0.003 m
Triangle width, w	0.007 m
Number of biofouling elements, N	24

Marine fouling in this work is presented by triangular elements resembling simplified barnacles in 2D with the height of 0.003 m, as given in Table 1. For a comparison, Table 2 shows some surface roughness heights and cylinder diameters in already published studies. In this current work, the triangular elements are assumed to be uniformly distributed around the cylinder similar to [10] even though marine fouling is non-uniform and randomly distributed. The triangular roughness elements in the current work are selected to provide a controlled, repeatable, and parametrically well-defined representation of surface fouling, enabling systematic investigation of how geometric protrusions modify response amplitude, vortex formation, and wake dynamics. The model may not capture localized flow interactions generated by clustered fouling, and the resulting wake structures may remain more coherent than those observed in heavily fouled offshore conditions. While this idealization does not replicate the detailed morphology of biological colonies, it captures the dominant hydrodynamic effects of biofouling, namely, enhanced flow separation, disruption of vortex coherence, and modification of wake dynamics.

Table 2. Surface roughness heights and structural diameters in the literature.

Studies	Surface Roughness Height, *h* (mm)	Diameter of Cylinder, *D* (mm)
[33]	0.4	160–400
[34]	20, 40	400
[35]	1.9–19	76.2
[36]	0.28–2	100

2.2. Flow Model

The flow around a cylinder is simulated by solving the transient, incompressible 2D Reynolds-Averaged Navier–Stokes (RANS) equation [37]. The mathematical formulation is as follows:

$$\frac{\partial(\rho\overline{u_i})}{\partial x_i} = 0, \tag{1}$$

$$\frac{\partial(\rho\overline{u_i})}{\partial t} + \frac{\partial}{\partial x_j}\left(\rho\overline{u_i u_j} + \rho\overline{u_i' u_j'}\right) = \frac{\partial\overline{p}}{\partial x_i} + \frac{\partial\overline{\tau_{ij}}}{\partial x_j} \tag{2}$$

where p represents the mean pressure, $\overline{u_i}$ means the average Cartesian components of the velocity vector, $\rho\overline{u_i' u_j'}$ are the Reynolds stresses, ρ is the density of the fluid, and $\overline{\tau_{ij}}$ is the mean viscous stress vector components, as follows:

$$\overline{\tau_{ij}} = \mu\left(\frac{\partial\overline{u_i}}{\partial x_j} + \frac{\partial\overline{u_j}}{\partial x_i}\right), \tag{3}$$

where μ denotes the dynamic viscosity.

The Shear Stress Transport (SST) k-ω turbulence model proposed by [38] is utilized to approximate the eddy viscosity which is well known for its predictive capability in flows experiencing adverse pressure gradients. The local eddy viscosity coefficient is computed in this model using both k-ω and k-ε formulations, depending on the wall proximity.

The authors acknowledge that the use of a Reynolds-Averaged Navier–Stokes (RANS) framework with the SST k–ω turbulence model imposes inherent limitations on the resolution of unsteady wake dynamics associated with vortex-induced vibrations. By construction, RANS models rely on time-averaged turbulence closures, which can lead to smoothing of transient flow structures, attenuation of small-scale turbulence, and partial suppression of peak unsteady force fluctuations. These effects are particularly relevant in regimes characterized by a strong flow separation, energetic vortex shedding, and high Reynolds numbers, such as those encountered during a lock-in. As a consequence, the SST k–ω model may under-predict instantaneous lift and drag force amplitudes and, therefore, yield conservative estimates of peak in-line and cross-flow vibration amplitudes, especially for smooth cylinders exhibiting a strong synchronization. In addition, the coherence and strength of individual vortices in the near wake may be modified relative to higher-fidelity approaches such as Large Eddy Simulations (LES) or Direct Numerical Simulations (DNS). These limitations should be taken into account when interpreting the absolute values of oscillation amplitudes and force coefficients reported in this study. Nevertheless, it can be emphasized that 2D RANS models are already used for this range of the Reynolds number [39], and the primary objective of the present work is to investigate relative trends, *KC*-dependent behavior, and comparative response modification due to biofouling. Since both smooth and biofouled configurations are simulated within the same turbulence modeling framework, the comparative conclusions regarding lock-in characteristics, amplitude saturation, and wake disruption remain physically meaningful and robust. The dominant large-scale vortex dynamics governing synchronization and response trends are reasonably captured within the SST k–ω RANS approach. For applications requiring precise quantitative prediction of peak vibration amplitudes or fatigue-relevant loads, fully three-dimensional simulations employing scale-resolving turbulence models (e.g., LES or hybrid RANS–LES methods) would be required and are identified as a natural extension of the present work.

ANSYS Fluent 2025 R1 software is used for all simulations. Finite Volume Method (FVM) is adopted in the software for the discretization of governing equations. The Green Gauss Cell Based method discretizes gradients, while Second Order and Second Order Upwind schemes are used for the pressure and momentum, respectively.

The PISO algorithm is employed in the current work following the study [40]. This method is found to be more robust, delivering a fully coupled solution for pressure and velocity at each time step while enforcing a divergence-free velocity field.

A User-Defined Function (UDF) controls the dynamic mesh to simulate each cylinder's motion. Smoothing and remeshing techniques are applied to the dynamic mesh cells. Initially, each cylinder is stationary in its equilibrium position in the origin of the coordinate system.

The fluid velocity $U(t)$ of the oscillatory flow is expressed as

$$U(t) = U_m \cos\left(\frac{2\pi t}{T}\right) \tag{4}$$

where t is simulation time, and U_m and T are the amplitude and period of the oscillatory flow velocity, respectively.

The *KC* number is determined based on the amplitude of the oscillatory flow velocity:

$$KC = \frac{U_m T}{D} \tag{5}$$

The effective *KC* number is expressed as:

$$KC_{eff} = \frac{U_{rel} T}{D}, \tag{6}$$

where U_{rel} is the velocity of the fluid motion in the in-line direction relatively the cylinder.

The relative velocity of the fluid motion is defined as:

$$U_{rel}(t) = U_m \cos\left(\frac{2\pi t}{T}\right) - \frac{dX}{dt} \tag{7}$$

where X is the in-line displacement of the cylinder, and $\frac{dX}{dt}$ is the in-line velocity of the cylinder.

Finally, the Reynolds number of the oscillatory flow is as follows:

$$Re = \frac{U_m D}{\nu}, \tag{8}$$

where ν is the kinematic viscosity of the fluid.

2.3. Structural Model

The 2DOF circular cylinder with and without biofouling is assumed elastically mounted, and its motion is simulated closely following the vibration model in the work [41]:

$$m_s\ddot{X} + c\dot{X} + kX = F_X, \tag{9}$$

$$m_s\ddot{Y} + c\dot{Y} + kY = F_Y, \tag{10}$$

where m_s denotes the structural mass per unit length, c is the damping coefficient per unit length, k is the stiffness coefficient of the elastic support per unit length, F_X, F_Y are unsteady hydrodynamic forces acting in the in-line and transverse directions per unit length produced by the oscillatory flow, and Y is the cross-flow displacement of the cylinder.

Equation (11) defines the mass ratio m^* of the circular cylinder:

$$m^* = \frac{m_s}{m_{fd}}, \tag{11}$$

where

$$m_{fd} = \frac{\pi D^2 \rho}{4}, \tag{12}$$

where m_{fd} represents the mass of the displaced fluid per unit length.

In the current study, the smooth and biofouled cylinders are assumed to have the same mass ratio m^*, damping coefficient c and stiffness coefficient k. So that, all observed differences in the dynamical behavior of two structures arise from the difference in the fluid forcing F_X, F_Y, defined by geometrical shapes, as computed by the software for each time step.

Equation (13) expresses the relation for determining the system's reduced velocity U_r:

$$U_r = \frac{U_m}{f_n D}, \tag{13}$$

where f_n is given by

$$f_n = \frac{1}{2\pi}\sqrt{\frac{k}{m_{eff}}}, \tag{14}$$

where

$$m_{eff} = \frac{\pi D^2 \rho_f}{4} C_A + m_s. \tag{15}$$

In the current work, the added mass coefficient C_A is taken as 1 for simplicity, according to the classical hydrodynamic theory and common CFD practice.

The effective reduced velocity is defined as

$$U_{r_{eff}} = \frac{U_{rel}}{f_n D}. \tag{16}$$

2.4. Computational Domain and Boundary Conditions

The computational domain used in the current work spans $63D \times 43D$, as illustrated in Figure 1a. The center of gravity of the cylinder at the beginning of the simulation is located at $23D$ from the inlet, which is a velocity-inlet with oscillatory flow velocity U:

$$u(x = -23D, y, t) = U, v(x = -23D, y, t) = 0. \tag{17}$$

The right boundary of the domain at $x = 40D$ is the outlet, where a zero-gauge pressure is prescribed, and convective (zero-gradient) conditions are applied for the velocity components:

$$p(x = 40D, y, t) = 0, \; \frac{\partial u}{\partial x}(x = 40D, y, t) = 0, \frac{\partial v}{\partial x}(x = 40D, y, t) = 0 \tag{18}$$

The top and bottom boundary are prescribed to be symmetry, following [42], such that

$$v(x, y = 21.5D, t) = 0, \; \frac{\partial u}{\partial y}(x, y = 21.5D, t) = 0, \tag{19}$$

$$v(x, y = -21.5D, t) = 0, \; \frac{\partial u}{\partial y}(x, y = -21.5D, t) = 0, \tag{20}$$

The no-slip condition is imposed on the surface of the cylinder.

2.5. Verification and Validation of the Numerical Model

The computational domain is discretized using an unstructured triangular mesh similar to the work of [43]. The surface of the cylinder is designed to have an O-shaped mesh with a finer grid resolution in order to capture the flow features in this region. To ensure $y^+ \leq 1$, the first layer cell height of 0.000025 m is employed.

Mesh and time convergence studies are conducted to ensure the accuracy of results. The mesh independence study is performed for a 1DOF motion of a biofouled cylinder on four different meshes using the same structural parameters, as outlined in [10] and Table 3. Results for these studies are presented in Tables 3 and 4, with Grid 3 selected for further simulations. Resolution of this mesh is demonstrated in Figure 1b,c for the smooth and biofouled cylinders, respectively. Results in Table 4 allow selecting the time step size of 0.005 s to obtain solutions on this mesh.

Table 3. Mesh independence test results.

Grid	Number of Mesh Volumes	Number of Biofouling Elements	Height of Biofouling Elements	U_r	m^*	A_y/D
			Current study			
Grid 1	60,751	24	0.003	7	4.8	0.458
Grid 2	67,707					0.450
Grid 3	74,750					0.453
Grid 4	80,387					0.455
			Published data			
[10]	-	24	0.003	7	4.8	0.460

Table 4. Time step convergence test results.

Grid	Number of Mesh Volumes	Time Step	Number of Biofouling Elements	Height of Biofouling Elements	U_r	m^*	A_y/D
			Current study				
Grid 3	74,750	0.01	24	0.003	7	4.8	0.471
Grid 3	74,750	0.005					0.453
Grid 3	74,750	0.004					0.457
			Published data				
[10]	-		24	0.003	7	4.8	0.46

Further simulations are performed to validate the numerical model for 2DOF VIV of an elastically mounted smooth circular cylinder using the same parameters as those of [44], as presented in Table 5. Figure 2 shows the response amplitudes obtained in the present study and the numerical results of [44], and the presented results are in a good agreement.

Table 5. Parameters for validation test.

Grid	**Number of Mesh Volumes**	**Frequency, f_n**	**Mass Ratio, m^***	**Damping Ratio, ζ**	**Diameter, D**
			Current study		
Grid 3	74,750	0.4 Hz	2.6	0.0036	0.043
			Published data		
[44]	72,400	0.4 Hz	2.6	0.0036	0.043

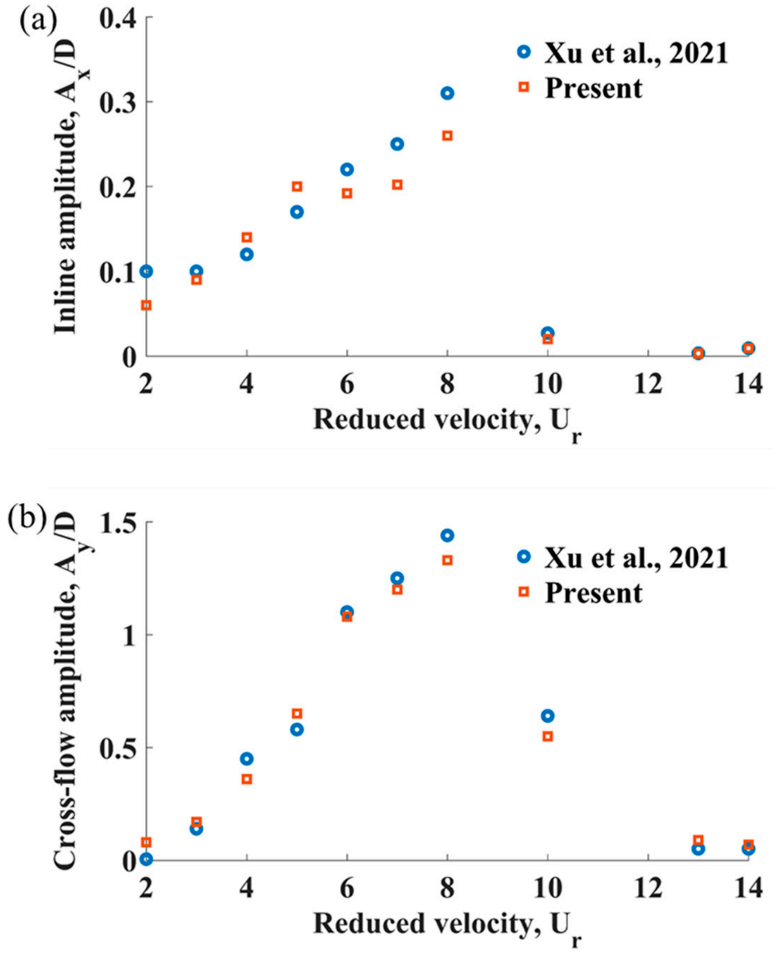

Figure 2. Comparison of maximum displacement amplitudes with [44]: (**a**) in the in-line direction; (**b**) in the cross-flow direction.

Also, the numerical model is validated against [45] for an elastically mounted smooth 2DOF cylinder in an oscillatory flow at a *Re* = 5000 and *KC* = 5 using a mass ratio and damping ratio of 2 and 0, respectively, for a range of reduced velocities from 2–8. The results presented in Figure 3 show good agreement with the published data.

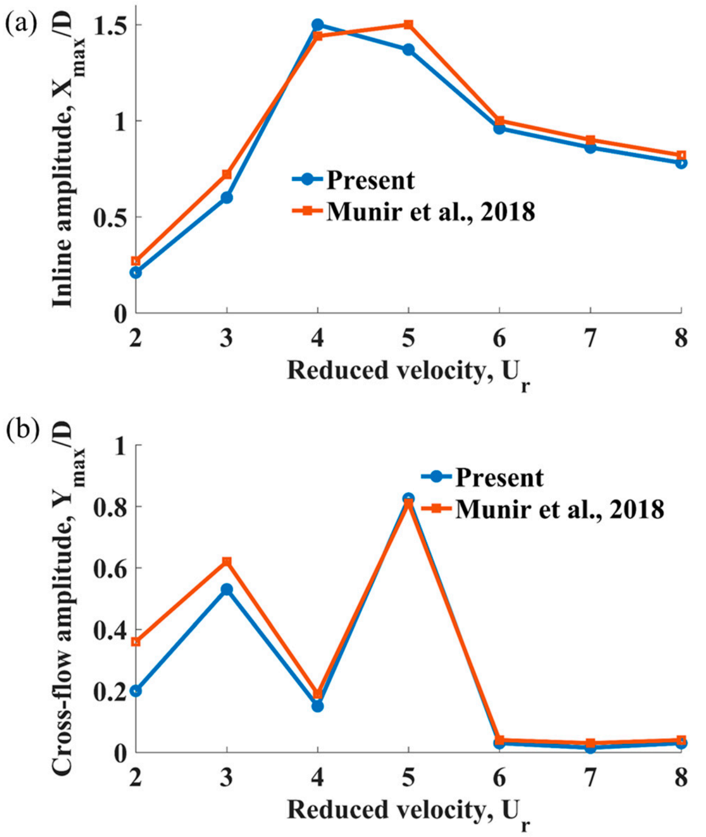

Figure 3. Comparison of maximum displacement amplitudes with [45]: (**a**) in the in-line direction; (**b**) in the cross-flow direction.

3. Results

The current work investigates the effect of *KC* numbers on a single smooth and biofouled cylinder with two degrees of freedom in an oscillatory flow. Effects of selected *KC* numbers on the response amplitude, frequency ratios, lock-in, *XY* trajectories and vorticity contours are presented below.

3.1. Response Amplitude and Frequency Ratios for KC = 5

Figures 4 and 5 illustrate maximum response amplitudes and frequency ratios for the considered cylinders as a function of reduced velocity. Vibration amplitudes are calculated from the time histories of cylinders' displacements over 20 periods of oscillatory flow. Vibration amplitudes are defined as $A_x = \frac{X_{max} - X_{min}}{2}$ and $A_y = \frac{Y_{max} - Y_{min}}{2}$. The work [45] defines the lock-in range of reduced velocity as the interval between the beginning reduced velocity of the first lock-in peak and the ending reduced velocity of the last lock-in peak when multiple peaks of a lock-in occur. For *KC* = 5, the lock-in range is found to be $2 < U_r \leq 6$. The observed lock-in range is narrow, as expected for low *KC* numbers, because the limited flow reversal hinders the full development of organized vortex shedding cycles. Experiments in [10,46] reveal a decrease in the cross-flow amplitude of a biofouled cylinder compared to a smooth cylinder. Similarly, a substantial reduction in the cross-flow amplitude at *KC* = 5 for the biofouled cylinder is observed at U_r = 5 in the current work, where lock-in occurs for both cylinders. According to [47], the transverse amplitude in the "super-upper" branch can reach as high as 1.5*D*. A maximum cross-flow amplitude of 0.98*D* is reached by the smooth cylinder at U_r = 5 where the cross-flow vibration frequency (f_y), the structural natural frequency (f_n) and frequency of the oscillatory flow (f_w) synchronize. For the biofouled cylinder, the maximum cross-flow amplitude is significantly lower and is observed earlier in the reduced velocity range at U_r = 3. For both cylinders at *KC* = 5, the cross-flow vibration amplitude begins to cease from U_r = 6, which is similar to the observation made in [45].

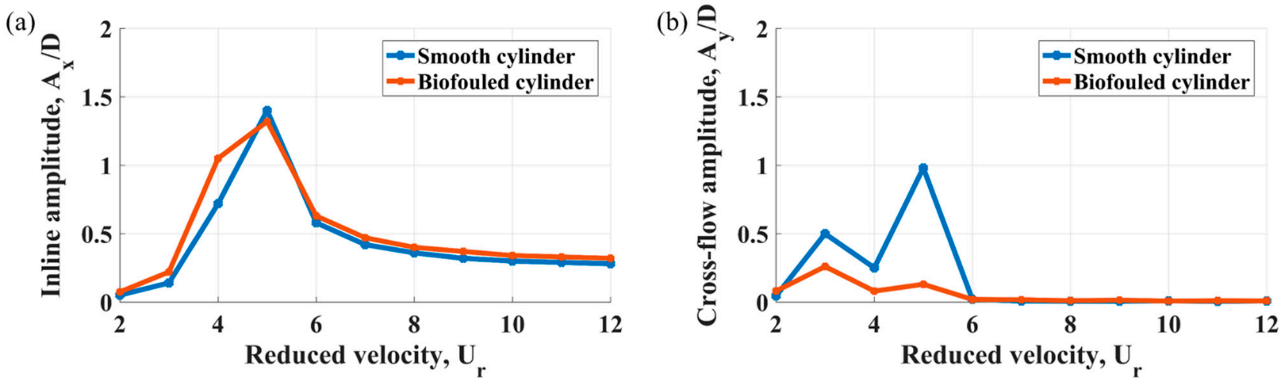

Figure 4. Maximum displacement amplitudes at *KC* = 5: (**a**) in the in-line direction; (**b**) in the cross-flow direction.

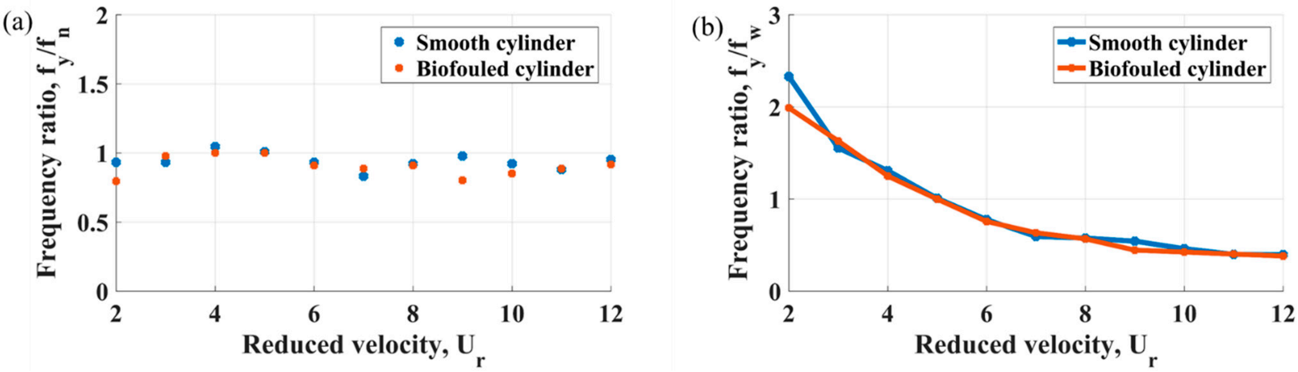

Figure 5. Frequency ratios of the cylinders at *KC* = 5: (**a**) f_y/f_n (**b**) f_y/f_w.

The in-line amplitude of the biofouled cylinder overall is observed to be higher than that of the smooth cylinder. However, the maximum in-line amplitude of 1.4*D* at U_r = 5 is recorded for the smooth cylinder where the lock-in occurs.

For *KC* = 5 at $2 \leq U_r \leq 3$, the cross-flow displacement exceeds the in-line displacement. However, beyond this reduced velocity, the in-line displacement becomes larger than the cross-flow displacement, and the difference between the two increases with increasing reduced velocity. This is consistent with the work of [48].

At *KC* = 5, the oscillatory flow frequency matches the vibration frequency in the in-line direction. A Fast Fourier Transform (FFT) is applied to analyze the frequency content of the transverse vibration amplitude. For oscillatory flow, the oscillatory frequency is defined as $f_w = \frac{1}{T}$ where *T* is the period of the oscillatory flow. In this current work, two transverse vibration frequency (f_y) ratios are defined in terms of the structural natural frequency (f_n) and oscillatory flow frequency (f_w). Synchronization occurs at U_r = 5 for both cylinders. The cross-flow vibration frequency for the smooth cylinder is found to be a bit higher compared to that of the biofouled cylinder, similar to [49], which could be linked to a higher effective diameter of the biofouled cylinder [10].

Studies [50–52] reveal that, for pure oscillatory flow, the cross-flow vibration occurs at frequencies that are integer multiples of the oscillatory flow frequencies. The work [18] classifies the vibration mode based on the dominant frequency. The single-frequency mode occurs when vibration matches the flow frequency, and the double-frequency mode occurs when it is twice the flow frequency. In Figure 5b, a single frequency mode is observed for both cylinders at U_r = 5.

Figure 6 illustrates the maximum effective reduced velocity and the effective KC number for both cylinders as a function of reduced velocity. A key observation from this figure is the sharp, single-step decrease in both $U_{r_{eff}}$ and KC_{eff} occurring precisely at U_r = 6. This abrupt change is a direct consequence of the cylinder's in-line motion falling into a perfect synchronization with the oscillatory flow. At this specific reduced velocity, the phase difference between the fluid velocity and the cylinder's inline velocity approaches zero. When the motions are in-phase, the relative velocity U_{rel} (Equation (7)), which is the driving factor for vortex shedding, minimizes. This causes the sudden collapse of $U_{r_{eff}}$ and KC_{eff}. For KC = 5, the limited flow excursion length means the system has a narrow window of vulnerability to VIV. Once this specific in-line lock-in condition is met at U_r = 6, the vortex shedding mechanism is effectively "switched off," leading to the cessation of cross-flow vibrations beyond this point [45].

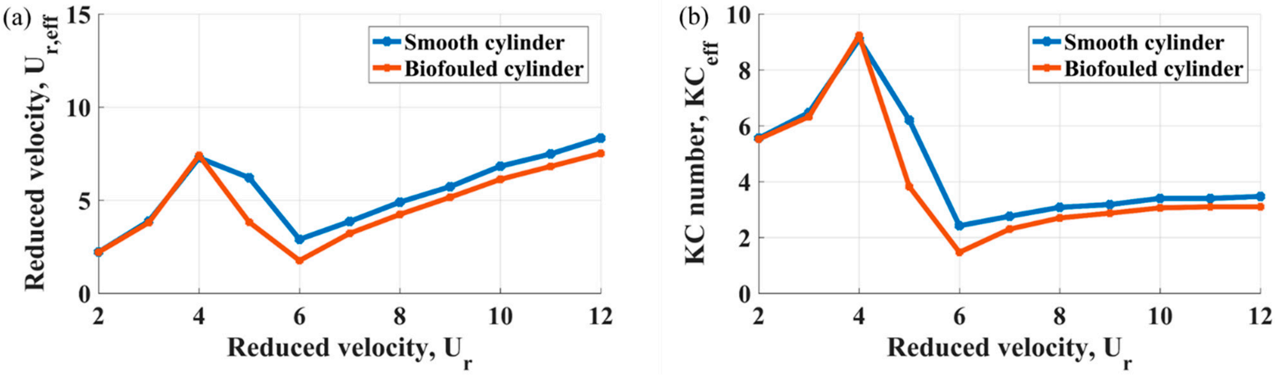

Figure 6. Effective variables of the cylinders at KC = 5: (**a**) effective reduced velocity; (**b**) effective KC_{eff} number.

3.2. Response Amplitude and Frequency Ratios for KC = 10

Figures 7 and 8 illustrate the response amplitudes and frequency ratios of the considered cylinders at KC = 10 as a function of reduced velocity. At KC = 10, the lock-in occurs at $5 \leq U_r \leq 10$ with the maximum vibration amplitude experienced at U_r = 10 for the cross-flow direction. At U_r = 5, the lock-in occurs for the biofouled cylinder, and the cross-flow vibration matches the natural frequency of the structure. At U_r = 10, the lock-in is still observed for both cylinders, and the cross-flow vibration frequency matches the natural frequency of the structure and the oscillatory flow frequency. The lock-in regime for KC = 10 is, therefore, slightly wider, compared to KC = 5.

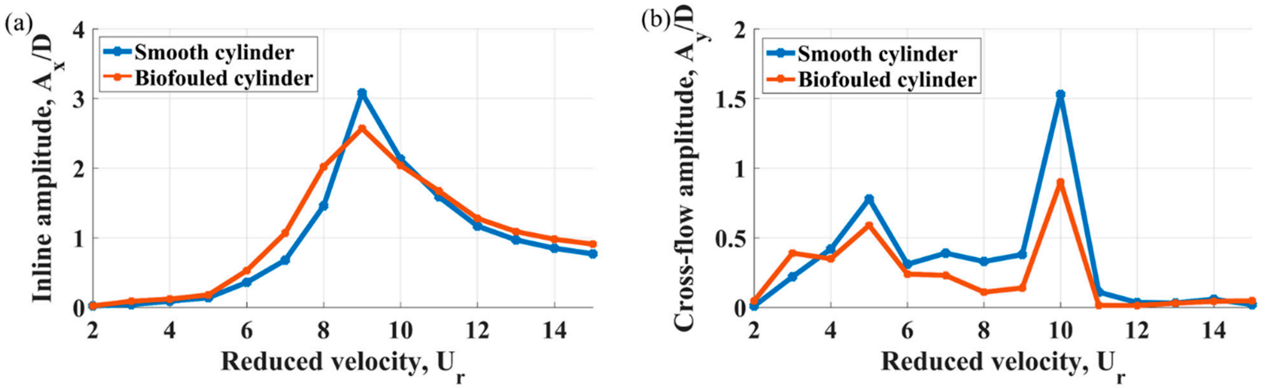

Figure 7. Maximum displacement amplitudes at KC = 10: (**a**) in the in-line direction; (**b**) in the cross-flow direction.

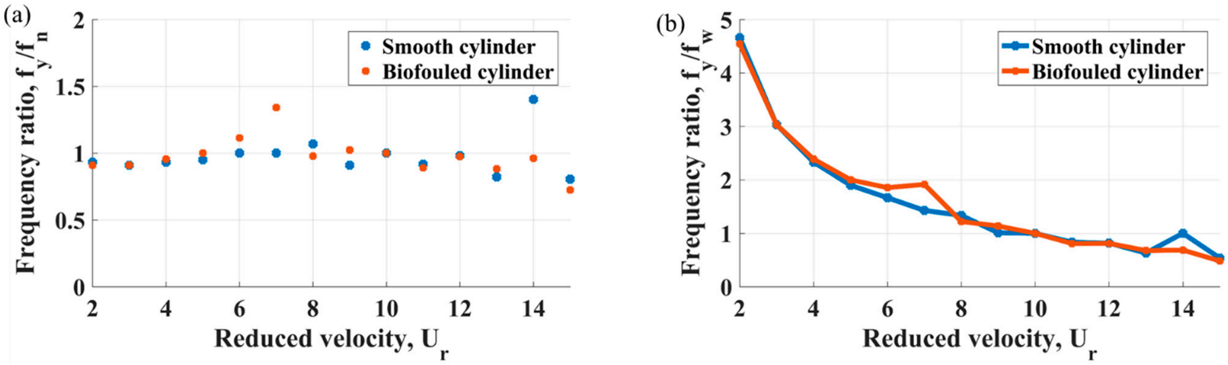

Figure 8. Frequency ratio of the cylinders at $KC = 10$: (**a**) f_y/f_n; (**b**) f_y/f_w.

Compared to $KC = 5$, the vibration amplitudes at $KC = 10$ is much higher for both cylinders with the smooth cylinder recording the maximum vibration amplitude of $1.54D$. The higher amplitudes compared to $KC = 5$ are expected. A larger KC number implies a longer fluid particle excursion, allowing for the formation of stronger and more organized vortex structures within each half-cycle. Stronger vortices impart greater impulsive forces on the cylinder, leading to larger vibrations.

A drop in the cross-flow amplitude is observed for both cases at $5 < U_r \leq 9$. These lowest amplitudes are due to the desynchronization of the cross-flow vibration amplitude with the natural frequency of the structure. The cross-flow vibration ceases with the reduced velocity exceeding 11 for all cases.

A trend, similar to $KC = 5$, is also observed for $KC = 10$ for the in-line response amplitude, where the largest in-line vibration amplitude belongs to the smooth cylinder. The in-line vibration amplitude is also observed to increase with the KC number. For $KC = 10$ at $2 \leq U_r \leq 5$, the cross-flow displacement exceeds the in-line displacement. However, beyond this reduced velocity, the in-line displacement becomes larger than the cross-flow displacement, and the difference between the two grows with the increasing reduced velocity.

For the considered cases, the cross-flow vibration frequency ratio, f_y/f_n stays close to 1. At $U_r = 5$ and 10, the vibration frequency synchronizes with the natural frequency of the structure. For the smooth cylinder, a single frequency mode occurs at $U_r = 10$, while, for the biofouled cylinder, a double frequency mode occurs at $U_r = 5$, and then a single frequency mode is further detected at $U_r = 10$.

Figure 9 illustrates the effective reduced velocity and effective KC number as a function of reduced velocity for $KC = 10$. It can be seen that for $KC = 10$, both the effective reduced velocity and the effective KC number reach their minimum values at $U_r = 11$. This explains why the vibration of the cylinder in the cross-flow direction ceases from $U_r = 11$.

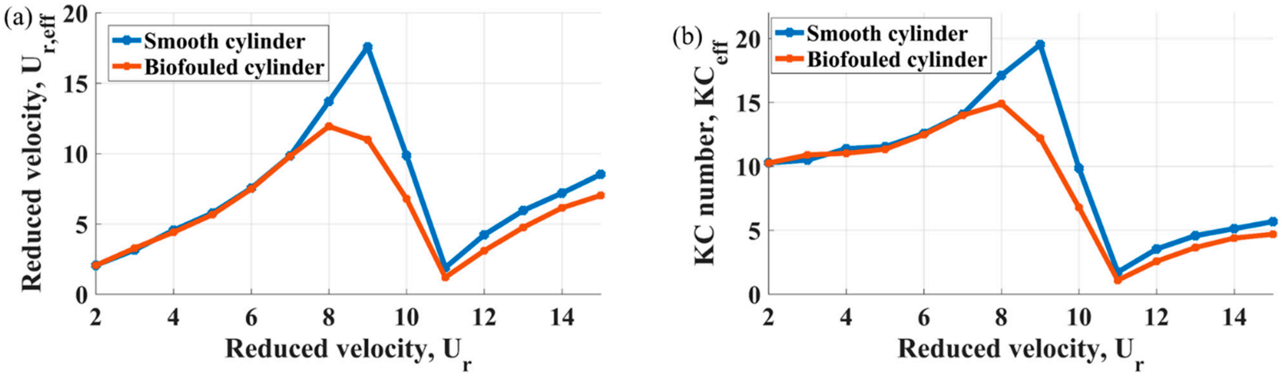

Figure 9. Effective variables at $KC = 10$: (**a**) effective reduced velocity; (**b**) effective KC_{eff} number.

3.3. Response Amplitude and Frequency Ratios for KC = 15

Figures 10 and 11 show the vibration response amplitude and frequency ratios for the considered cylinders at KC =15 as a function of reduced velocity. The maximum vibrating amplitude for the smooth cylinder is higher compared to the biofouled cylinder. For the smooth cylinder, the lock-in range is observed at $8 \leq U_r \leq 15$, and for the biofouled cylinder, it is observed at $6 \leq U_r \leq 15$. From results for KC numbers of 5, 10 and 15, it is possible to conclude that the vibration response amplitudes increase with the increasing KC number. The largest cross-flow amplitude of $1.8D$ is recorded for KC = 15 for the smooth cylinder, according to Figure 10b. It can be suggested that within the studied KC range (10 and 15), the peak cross-flow amplitude of the biofouled cylinder tends to change very little. While the roughness disrupts the vortex coherence, at high KC numbers, the flow inertia is sufficient to overcome this stabilization to some extent, but the vibration amplitude is capped well below that of the smooth cylinder. This has significant practical implications, indicating that biofouling may set an upper limit on VIV amplitudes regardless of the increasing flow severity. It is also worth noting that the cross-flow displacement frequency is close to the natural frequency of the structure for all KC numbers, which aligns well with findings of [28] for several KC numbers.

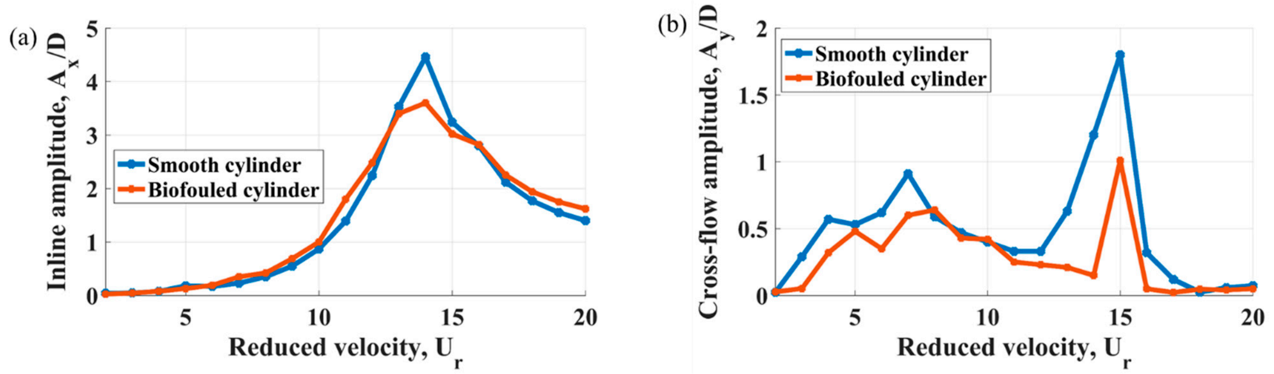

Figure 10. Maximum displacement amplitudes at KC = 15: (**a**) in the in-line direction; (**b**) in the cross-flow direction.

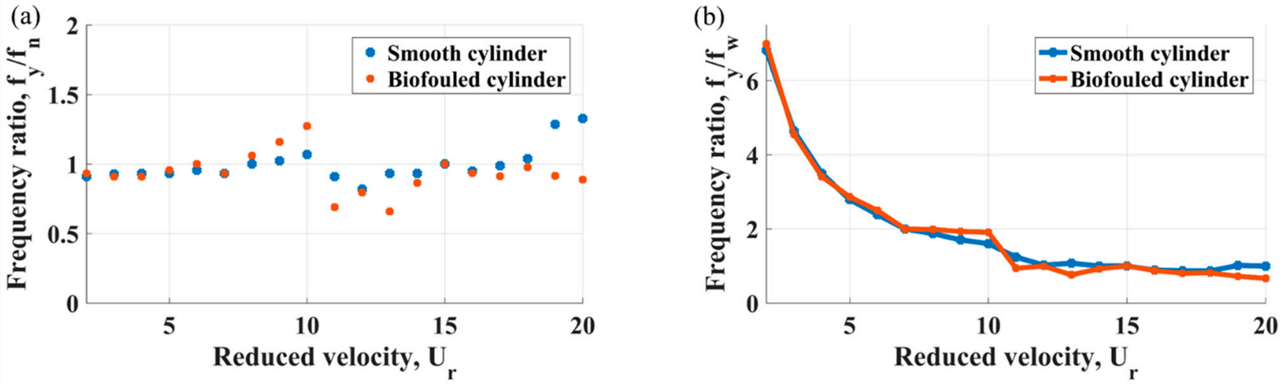

Figure 11. Frequency ratio of the cylinders at KC = 15: (**a**) f_y/f_n; (**b**) f_y/f_w.

A drop in cross-flow amplitude is observed for both cases at $8 < U_r < 13$. These lowest amplitudes result from a desynchronization of the cross-flow vibration amplitude with the natural frequency of the structure. The cross-flow vibration ceases with the reduced velocity exceeding 16 for all cases.

A maximum in-line amplitude of $4.46D$ at $U_r = 14$ is experienced by the smooth cylinder. For KC = 15 at $2 \leq U_r \leq 8$, the cross-flow displacement exceeds the in-line displacement. However, beyond this reduced velocity, the in-line displacement becomes

https://doi.org/10.3390/fluids11020055

larger than the cross-flow displacement, and the difference between them increases with the increasing reduced velocity, similar to the previously considered *KC* numbers. The overall comparison of maximum in-line and cross-flow amplitudes is shown in Table 6, where both largest in-line and cross-flow values belong to *KC* = 15 for either cylinder.

Table 6. Summary of the maximum cross-flow and in-line amplitude for both cylinders at the considered *KC* numbers.

Cases	***KC* = 5**		***KC* = 10**		***KC* = 15**	
	In-Line	**Cross-Flow**	**In-Line**	**Cross-Flow**	**In-Line**	**Cross-Flow**
Smooth cylinder	1.4	0.98	3.08	1.53	4.46	1.8
Biofouled cylinder	1.32	0.26	2.57	0.96	3.6	1.01

At $2 \leq U_r \leq 7$, there appear to be no significant difference in frequencies of two cylinders. However, as the reduced velocity increases from 8, a significant variation in the frequencies of cylinders is observed. At U_r = 8 and 15 for the smooth cylinder, the cross-flow vibration frequency matches the natural frequency of the structure, while for the biofouled cylinder, the cross-flow vibration synchronizes with the natural frequency of the structure at U_r = 6 and 15. A single frequency mode is observed for both cylinders at U_r = 15.

Figure 12 illustrates the effective reduced velocity and the effective KC number for the smooth and biofouled cylinder at *KC* = 15. It can be observed from the figure that the effective reduced velocity and *KC* number appear to be higher for the smooth cylinder than for the biofouled cylinder. Both the effective reduced velocity and the effective KC number reach their minimum values at U_r = 16. This explains why the vibration of the cylinder in the cross-flow direction ceases from U_r = 16.

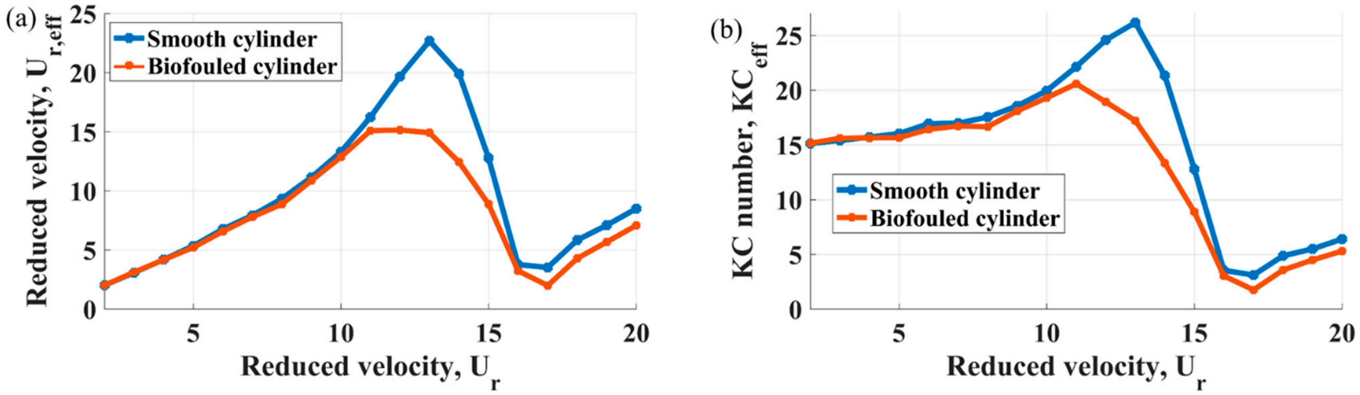

Figure 12. Effective variables at *KC* = 15: (**a**) effective reduced velocity; (**b**) effective *KC* number.

3.4. *XY Trajectories for KC Number = 5, 10 and 15*

Figures 13–15 depict the *XY* trajectories of considered cases at some selected reduced velocities for *KC* = 5, 10 and 15, respectively. For *KC* = 5 at $2 \leq U_r \leq 5$, figure-of-eight shape is described by the motion of the cylinders. At U_r = 5, a ring like-shape is observed for both cylinders, where the cross-flow vibration frequency, the frequency of the structure and the oscillatory flow frequency synchronized.

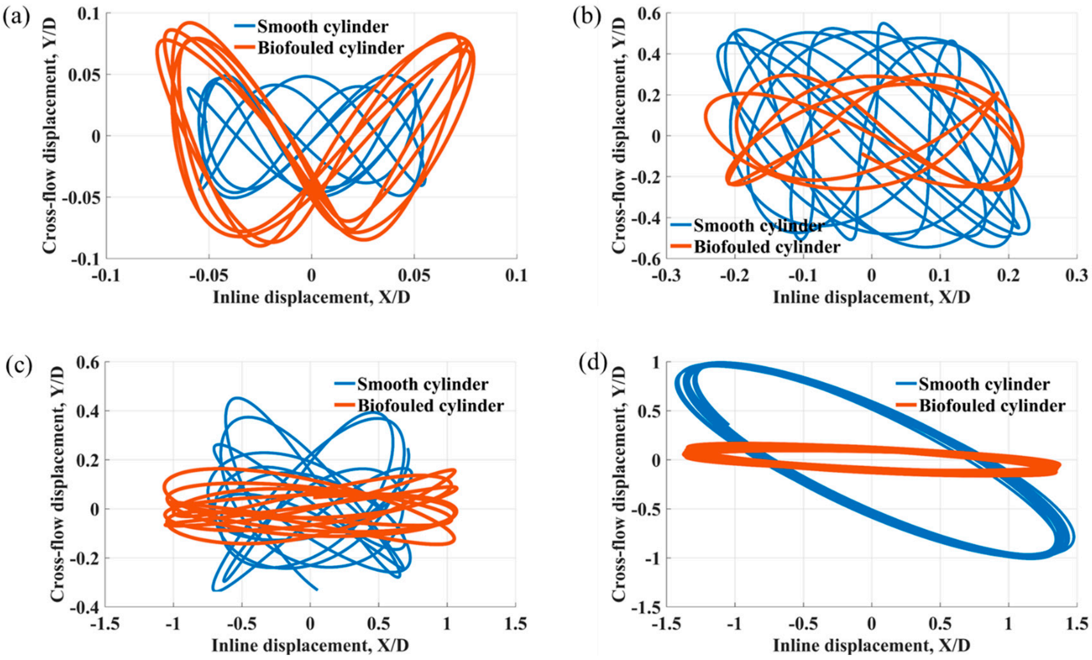

Figure 13. *XY* trajectory at $KC = 5$ for: (**a**) $U_r = 2$; (**b**) $U_r = 3$; (**c**) $U_r = 4$; (**d**) $U_r = 5$.

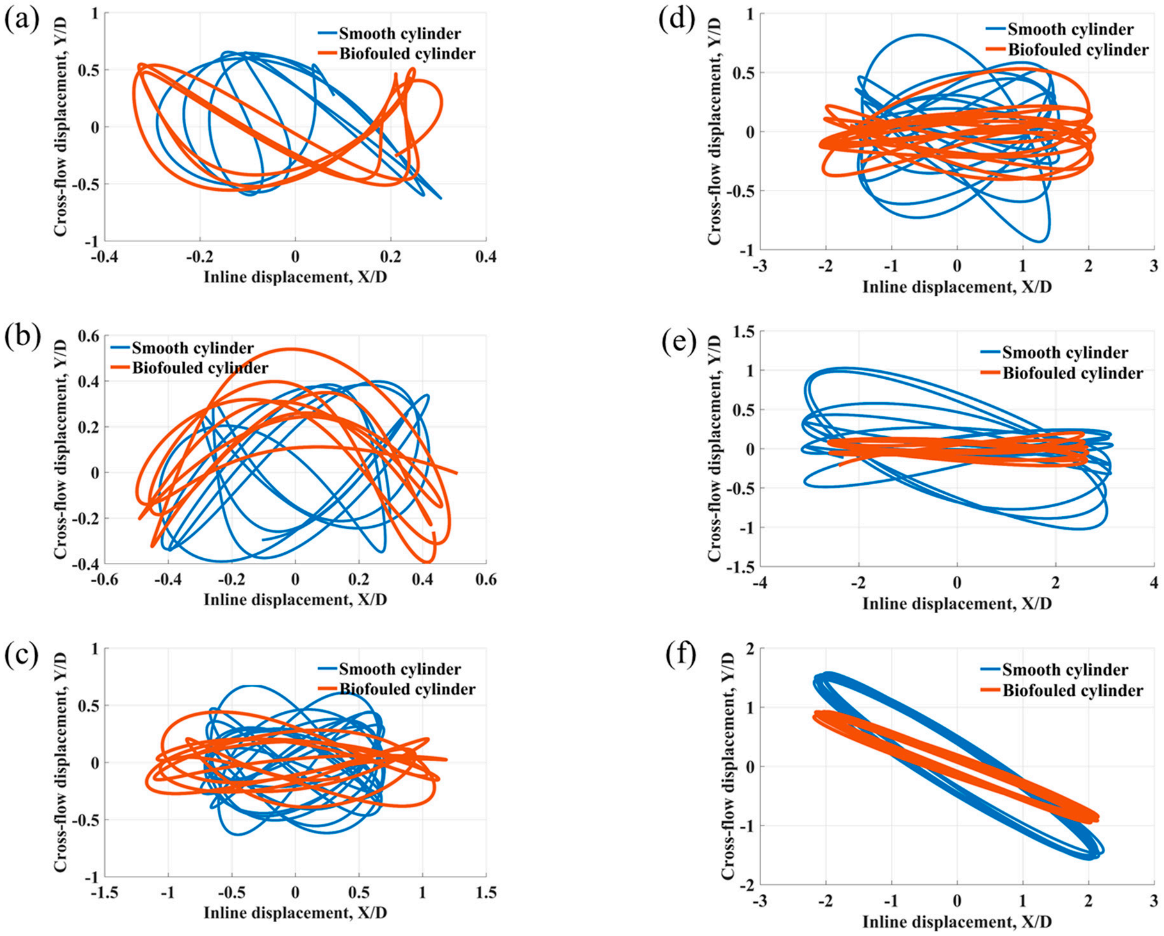

Figure 14. *XY* trajectories at $KC = 10$ for: (**a**) $U_r = 5$; (**b**) $U_r = 6$; (**c**) $U_r = 7$; (**d**) $U_r = 8$; (**e**) $U_r = 9$; (**f**) $U_r = 10$.

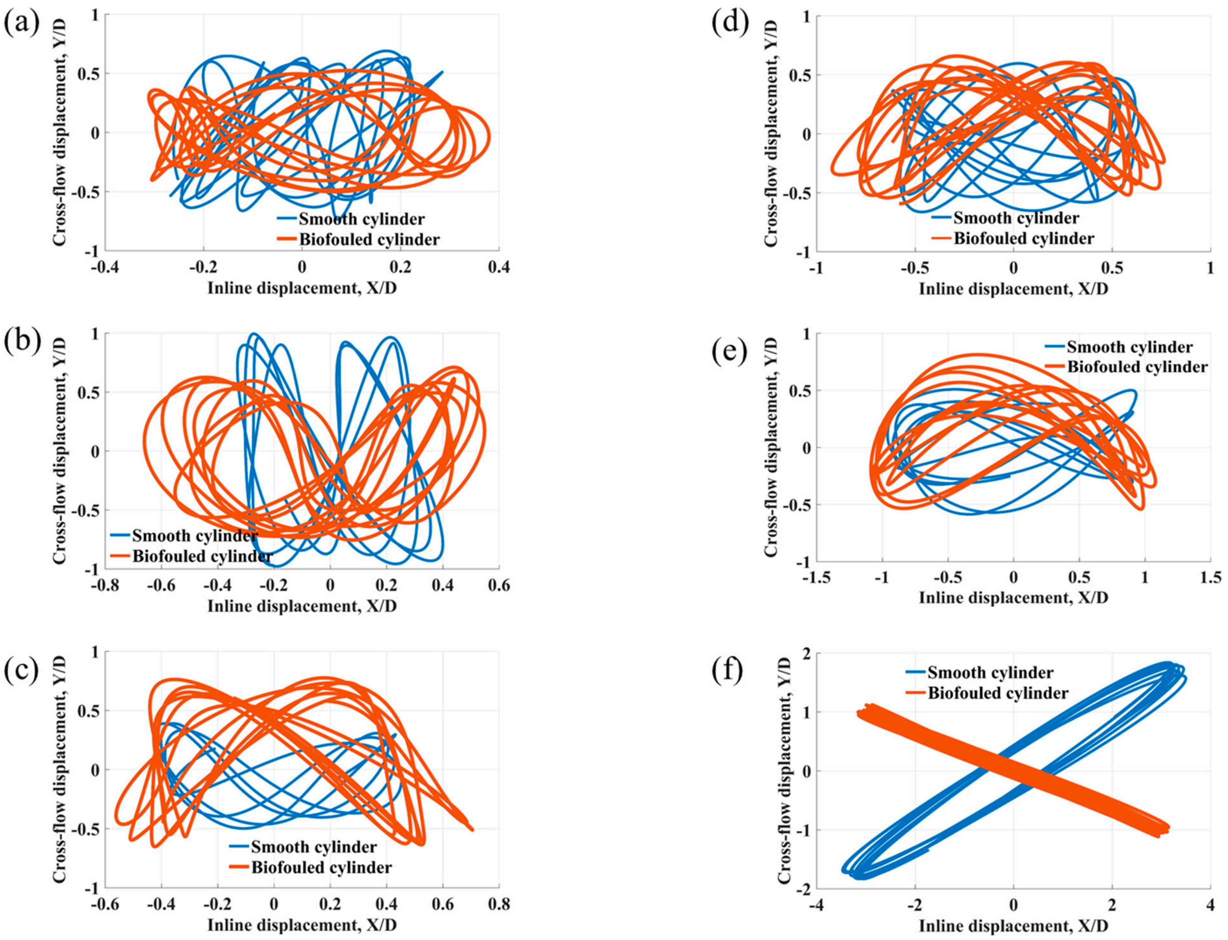

Figure 15. *XY* trajectories at *KC* = 15: (**a**) $U_r = 5$, (**b**) $U_r = 6$, (**c**) $U_r = 7$, (**d**) $U_r = 8$, (**e**) $U_r = 9$, (**f**) $U_r = 10$.

For *KC* = 10 at $U_r = 5$, both cylinders exhibit a well-defined figure-of-eight pattern which is classical for 2DOF VIV lock-in in oscillatory flow, where the vibration frequency is synchronized with the structural natural frequency (f_y/f_n) and is also approximately twice the flow frequency (f_y/f_w), corresponding to a double-frequency mode.

At $6 \leq U_r < 9$, the trajectories lose their organized structure, becoming irregular, elongated, or multi-looped. The cylinder is transitioning between synchronization modes. The fluid forces are fluctuating between these states, leading to a beat pattern or irregular motion in the response.

At $U_r = 10$, a well-defined arc-like shape is described by the cylinders. This shape is characteristic of a single-frequency mode, where the vibration frequency locks onto the oscillatory flow frequency. The motion is dominated by a large in-line component, with the cross-flow motion being nearly in-phase or with a small phase difference, resulting in this curved, primarily horizontal path. Beyond $U_r = 10$, the motion of the cylinder becomes entirely in-line dominated.

For *KC* = 15 at $6 \leq U_r \leq 10$, the motion of cylinders describes a well-defined figure-of-eight shape. At $U_r = 15$, a ring-like shape is described by both cylinders. The shape of the ring for the smooth cylinder is more open compared to the biofouled cylinder. Beyond $U_r = 16$, the in-line motion dominates.

3.5. Vorticity Contours

Figures 16–19 show vorticity contours for the smooth and biofouled cylinders at certain times within the flow at *KC* = 10 and 15.

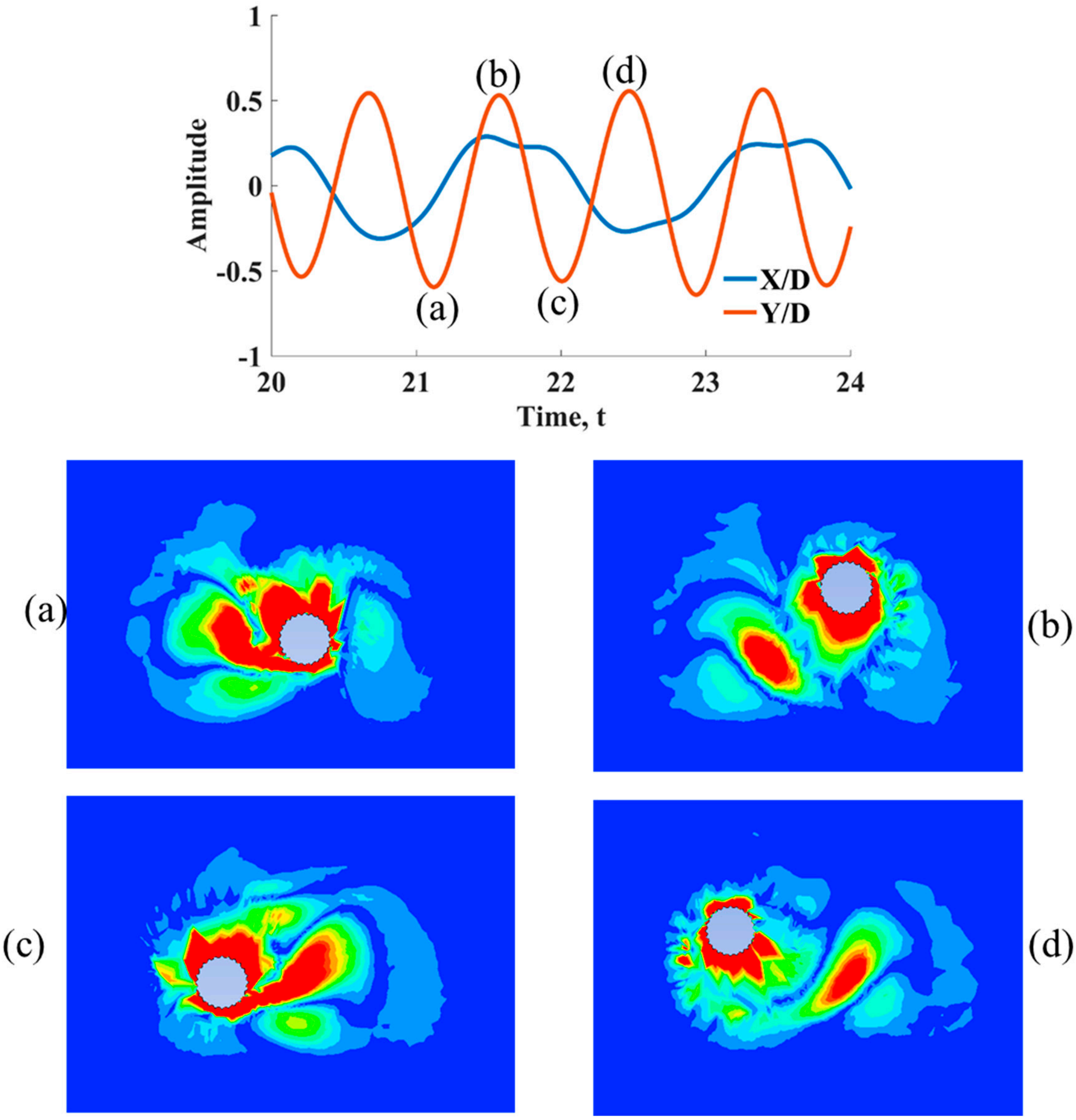

Figure 16. Vorticity magnitude contour for the biofouled cylinder at different stages of vibration cycle for KC = 10 at U_r = 5 at: (**a**) t = 21.13 s; (**b**) t = 21.57 s; (**c**) t = 22 s; (**d**) t = 22.47 s.

Figure 16 depicts the vortex shedding sequence for the biofouled cylinder at KC = 10 and U_r = 5—a condition identified as a double-frequency mode lock-in for this configuration. The sequence clearly shows the formation and subsequent shedding of a pair of vortices (2P mode) within a single half-cycle of the oscillatory flow. The presence of biofouling elements disrupts the smooth shear layer development, leading to an earlier detachment of vortices. This premature shedding results in vortices that are somewhat weaker and less coherent than those observed in the smooth cylinder case. This disrupted vortex formation process is the primary flow-level reason for the suppressed cross-flow vibration amplitudes observed for the biofouled cylinder, as weaker vortices impart lower impulsive transverse forces.

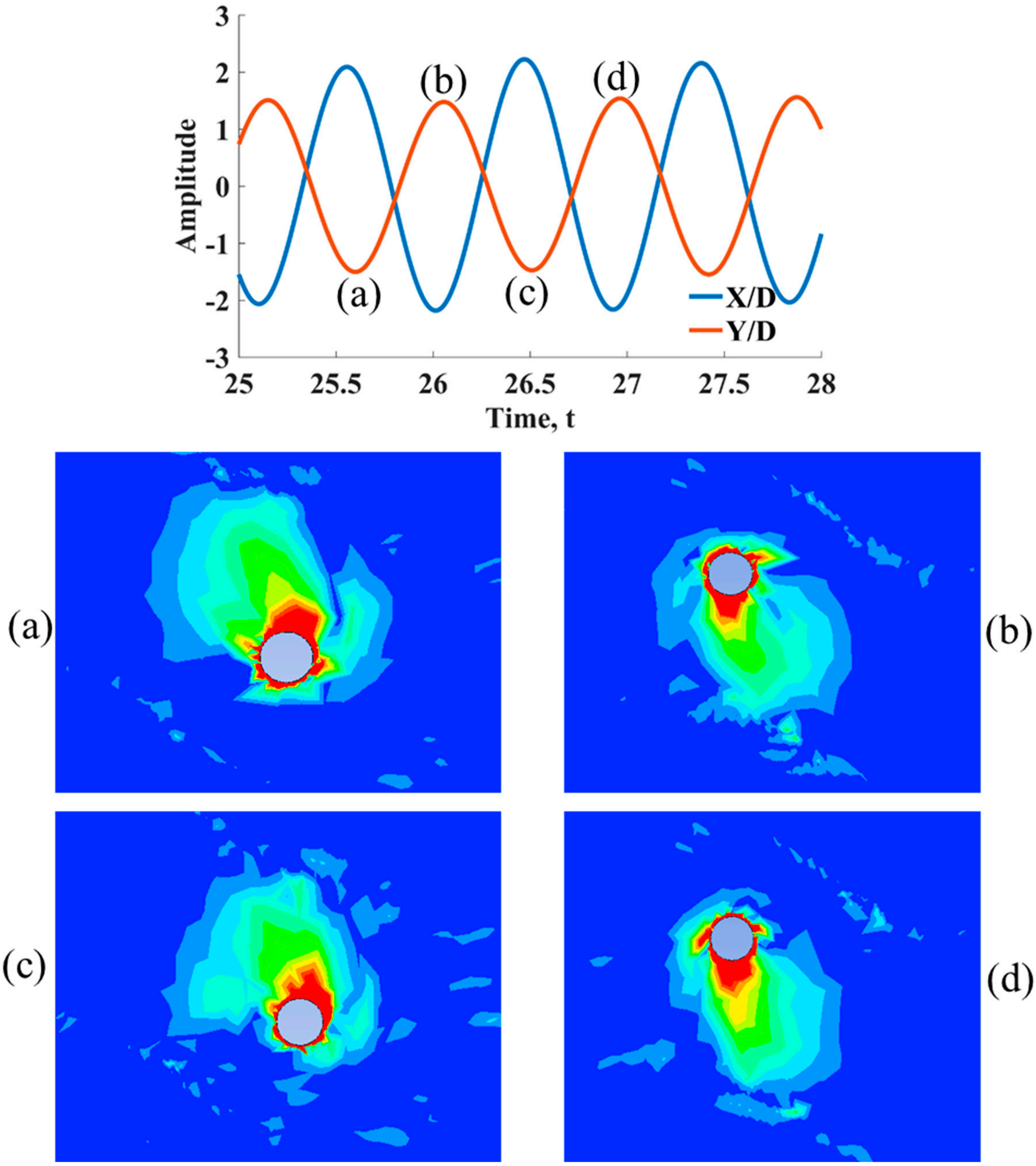

Figure 17. Vorticity magnitude contour for the smooth cylinder at different stages of vibration cycle for $KC = 10$ at $U_r = 10$ at: (**a**) $t = 25.59$ s; (**b**) $t = 26.05$ s; (**c**) $t = 26.53$ s; (**d**) $t = 26.96$ s.

Figure 17 shows the vorticity contour for the smooth cylinder at $KC = 10$ and $U_r = 10$, corresponding to its maximum amplitude single-frequency mode lock-in. Here, vortex shedding is characterized by a classical, strong, and well-organized 2S mode (two single vortices per cycle). The shear layers roll up into concentrated, high-strength vortices that are shed in a symmetric and periodic fashion. The coherence and strength of these vortex structures are directly responsible for the large, sustained cross-flow vibration amplitude (1.54D) achieved by the smooth cylinder. The clean separation points on the smooth surface allow for the full development of these powerful flow structures.

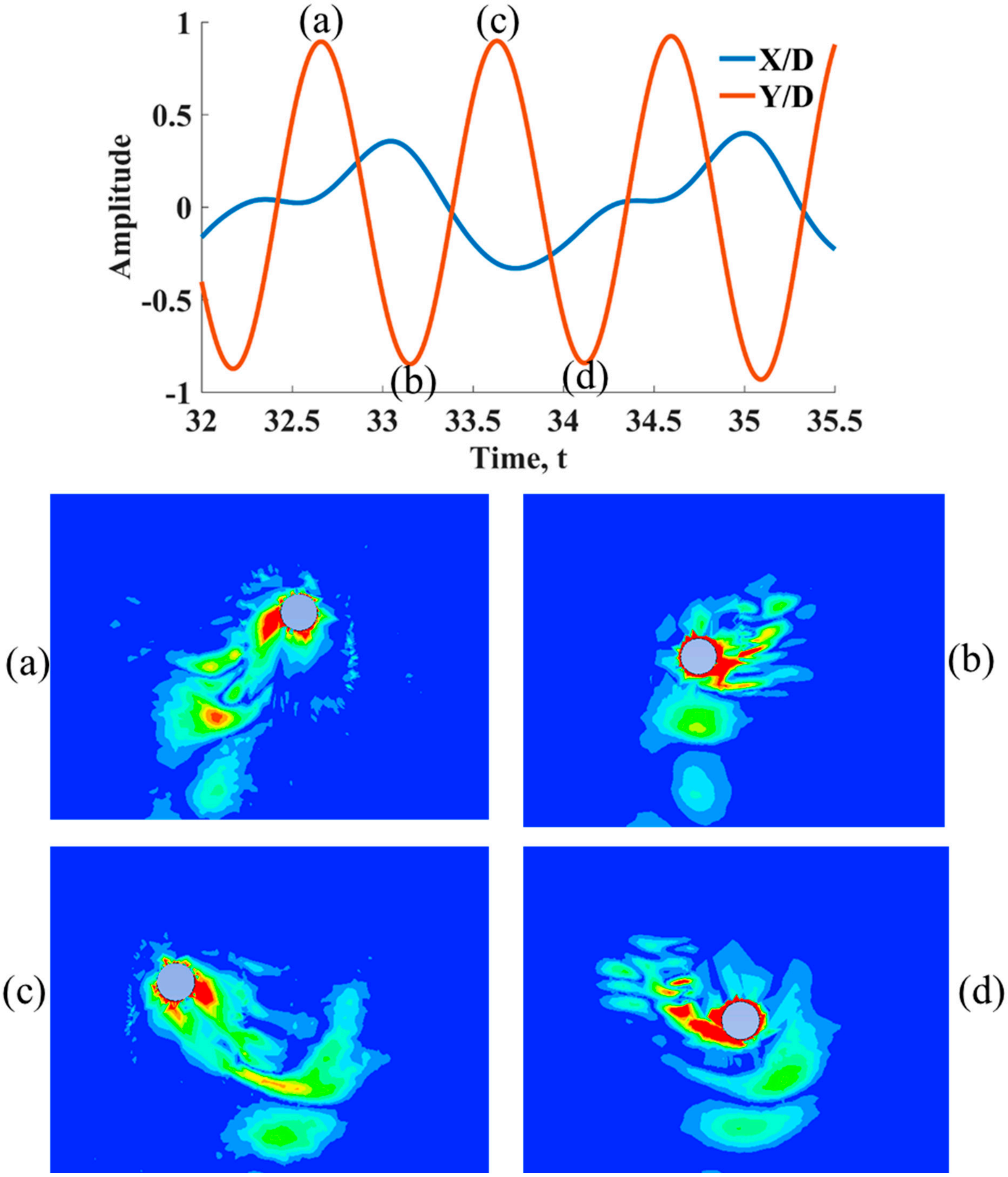

Figure 18. Vorticity magnitude contour for the smooth cylinder at different stages of vibration cycle for KC = 15 at U_r = 7 at: (**a**) t = 32.66 s; (**b**) t = 33.15 s; (**c**) t = 33.63 s; (**d**) t = 34.12 s.

Figure 18 for the smooth cylinder at KC = 15 and U_r = 7 (within its lock-in regime) demonstrates the effect of increased KC number. The longer fluid excursion allows for the formation of even larger and more intense vortex structures before flow reversal. The flow is able to organize itself into a very strong and correlated pattern, efficiently transferring energy to the cylinder.

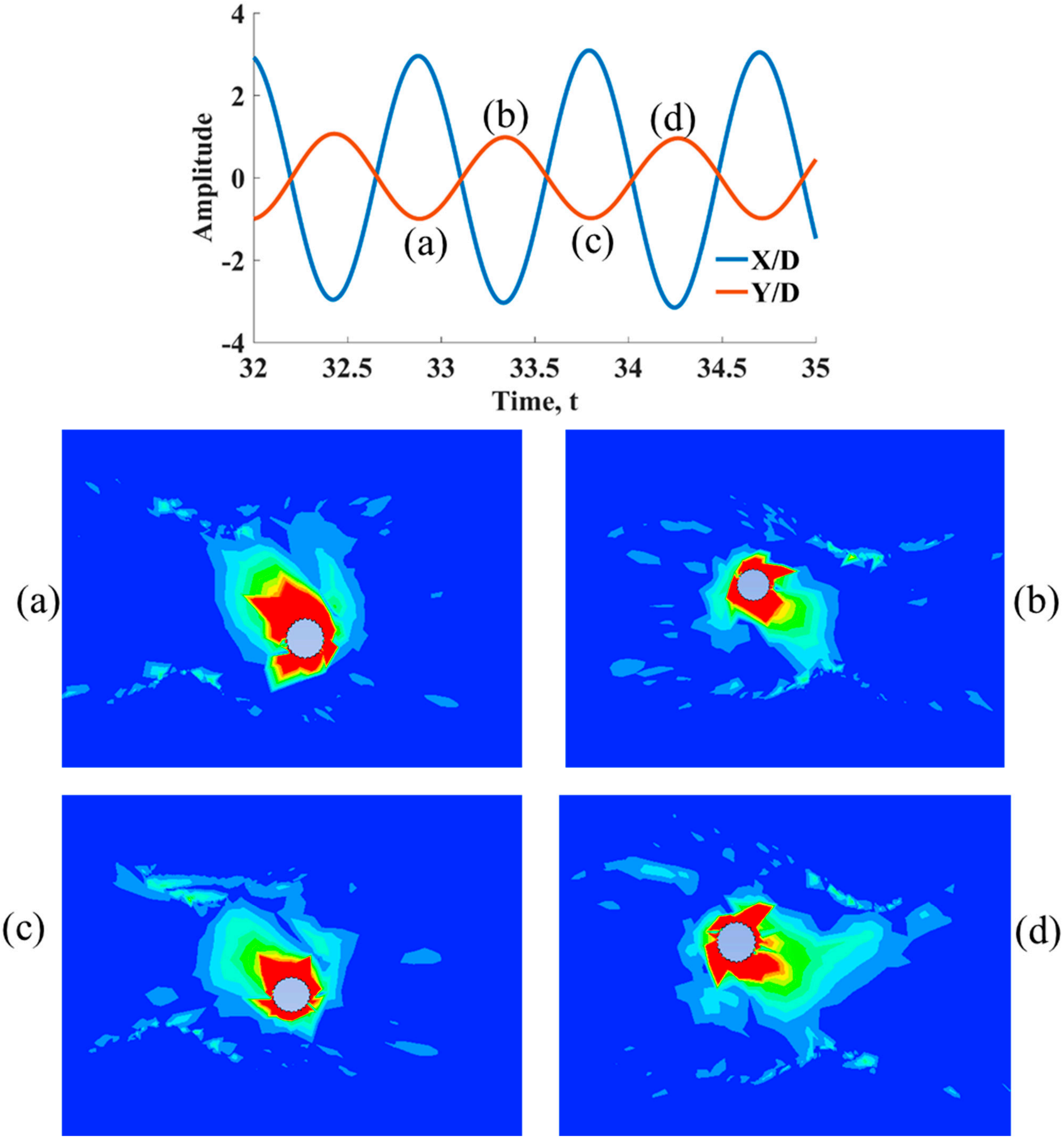

Figure 19. Vorticity magnitude contour for the biofouled cylinder at different stages of vibration cycle for KC = 15 at U_r = 15 at: (**a**) t = 32.87 s; (**b**) t = 33.34 s; (**c**) t = 33.79 s; (**d**) t = 34.25 s.

Figure 19 captures the biofouled cylinder at KC = 15 and U_r = 15, a condition of single-frequency mode lock-in. Despite the high KC number, which promotes strong vortex formation, the biofouling elements continue to exert a dominant influence. The vorticity field is significantly more disorganized compared to Figure 17. The wake is characterized by multiple small-scale vortical structures and a less distinct, more diffuse shedding pattern. This "scrambling" of the vortex street by the surface roughness prevents the build-up of highly correlated fluid forces, thereby capping the vibration amplitude. Even with sufficient flow energy (high KC), the biofouling effectively limits the organization of the wake, resulting in the observed amplitude almost plateauing around 1.0D.

3.6. Limitations, Perspectives and Practical Application

The current study has several inherent limitations, related to the numerical model set-up. It is worth emphasizing that results of the present work are valid only for the studied parameter range, specifically, for the selected Reynolds number of 9251–92,505, mass ratio of 4.8 and damping ratio of 0.005, which are governing quantities for the VIV phenomenon. Also, the investigation addresses only three Keulegan–Carpenter numbers. Findings from the current study could be projected on other parameter ranges with caution only, and would require additional simulations in majority of cases. The selected model approach essentially simplifies a complex 3D fluid–structure interaction phenomenon to a 2D space and uses RANS equations—a move supported by the substantial validation with published literature. Also, only uniform biofouling is taken into account in the present work, presented as triangular elements, following already published research, while the real fouling is non-uniform in the majority of real situations.

Perspectives of future research, from the authors' point of view, are strongly related to vibrational effects observed for arrays of biofouled structures in uniform and various complex flows. It would also be of benefit to the field of knowledge to investigate an impact of differences in the mass ratio, damping ratio and natural frequency between smooth and fouled structures on the vibrational response. The topic of VIV of objects with biofouling could also be extended towards 3D simulations of structures with non-uniform fouling, in order to cover ranges of structural and flow parameters, for which no experimental data are available.

Building on results of the present study, it would be also interesting to check the hypothesis about the upper limit of the peak cross-flow amplitude of a biofouled structure. In the current work, at $KC = 15$, the smooth cylinder achieves a large cross-flow amplitude of $1.8D$, while the biofouled cylinder shows approximately $1.0D$, which is similar to the amplitude level at $KC = 10$. This indicates that the amplitude-limiting effect of biofouling potentially reaches a saturation point, suggesting that roughness disrupts the coherence and strength of vortex shedding, thereby imposing an upper limit on VIV amplitudes regardless of an increasing flow severity. This observation requires additional checks of the VIV response of a biofouled cylinder at higher KC numbers, so that it could be confirmed if this is a significant pattern.

From the practical point of view of a subsea pipeline designer, results of this study confirm widening of the lock-in ranges in both directions in terms of the reduced velocity of the flow with the increase in the Keulegan–Carpenter number. This conclusion is valid for both structures, and could facilitate the respective choice of safety factors for a similar case. Also, a reasonable recommendation from the current analysis would be that designing subsea structures at reduced velocities lower than the lock-in condition is preferable, due to the onset of relatively large in-line displacement amplitudes in a post-lock-in range. These amplitudes reach $1D$ at $KC = 10$ and exceed this value at $KC = 15$, which constitutes a substantial fatigue load on the structure in an oscillatory flow.

4. Conclusions

This numerical study systematically investigates the two-degrees-of-freedom vortex-induced vibrations of both smooth and biofouled circular cylinders subjected to oscillatory flow, with a specific focus on the influence of the Keulegan–Carpenter number. By employing a validated RANS-based CFD model with the SST k-ω turbulence model, the research provides significant insights into the amplitude response, frequency synchronization, lock-in regimes, and trajectory patterns for KC numbers of 5, 10, and 15 over a reduced velocity range from 2 to 20.

Results indicate that peak in-line displacement amplitudes consistently exceed peak cross-flow displacement amplitudes for both structures, which is expected for the dynamics of slender structures in an oscillatory flow. Another central finding is that marine biofouling, modeled as triangular surface roughness, consistently suppresses the cross-flow vibration amplitudes across all investigated KC numbers. At the same time, a closer look at the in-line response suggests that, at the initial and concluding stages of the in-line lock-in, and also at post-lock-in, in-line displacement amplitudes of a biofouled structure are larger than in-line amplitudes of a bare structure. This creates a possibility of a more significant fatigue accumulation for a biofouled structure, depending on exact flow velocities.

As the KC number increases from 5 to 15 in the current work, the lock-in regime broadens significantly in the reduced velocity range. Concurrently, the maximum vibration amplitudes increase with the KC number and also tend to occur at higher reduced velocities within the lock-in range. It also should be noted that the maximum cross-flow displacement at $KC = 5$ for a biofouled structure is experienced very early in the reduced velocity range, compared to the bare structure at $KC = 5$ and the biofouled structure at other KC numbers. A peak cross-flow amplitude at $U_r = 3$ is not usual for VIV development in general, as the lock-in state is normally expected to occur at $U_r = 5$ for uniform flow cases with a bare structure.

Another interesting observation, related to KC numbers, is the near equality of peak cross-flow displacement amplitudes, expected for a biofouled structure at $KC = 10$ and $KC = 15$. As mentioned in Section 3.6, this pattern requires further evidence to be collected in future studies to confirm the range of amplitude stabilization in terms of the KC number for a biofouled structure.

The XY trajectories of the cylinders serve as a clear visual indicator of the lock-in state and frequency mode. Well-defined figure-of-eight shapes are observed during the lock-in in the double-frequency mode while ring-like or arc-like shapes characterize the single-frequency mode. Trajectories of the biofouled cylinder are often more irregular or constrained compared to the smooth cylinder, reflecting the disruptive impact of surface roughness on the regularity of vortex shedding, which is also supported by vorticity contours.

In summary, this work confirms that the presence of uniform biofouling substantially changes the lock-in development patterns, compared to a bare structure in oscillatory flow, which was not previously reported in the published literature, to the knowledge of the Authors. These findings have critical implications for the design and integrity assessment of offshore marine structures, such as risers, umbilicals and mooring lines, where biofouling is inevitable. Current results underscore the necessity of accounting for a surface roughness in predictive VIV models to avoid incorrect estimates of the fatigue life. Future work could extend this analysis to three-dimensional simulations, different Reynolds numbers, and a wider variety of biofouling morphology patterns.

Author Contributions: Conceptualization, methodology, formal analysis, investigation, validation, data curation, visualization, writing—original draft preparation, H.F.A.; writing—original draft preparation, writing—review and editing, supervision, funding acquisition, project administration, V.K. All authors have read and agreed to the published version of the manuscript.

Funding: Authors would like to acknowledge the support of the Ministry of Science and Higher Education of the Russian Federation, grant number FEWN-2024-0005.

Data Availability Statement: All data are provided within the article.

Acknowledgments: V.K. would like to thank A. Postnikov for the productive discussions on CFD simulations of 2DOF structures in uniform flow.

Conflicts of Interest: The authors declare no conflicts of interest.

References

1. Momber, A. *Corrosion and Corrosion Protection of Wind Power Structures in Marine Environments: Volume 1: Introduction and Corrosive Loads*; Academic Press: Cambridge, MA, USA, 2024.
2. Harandi, M.A.; Tamimi, V.; Zeinoddini, M.; Rashki, M.R.; Ashrafipour, H. Effects of soft marine growth on vortex-induced vibration: A comparative analysis with hard marine growth. *Appl. Ocean Res.* **2024**, *144*, 103906. [CrossRef]
3. Terry, L.A.; Picken, G.B. Algal fouling in the North Sea. In *Studies in Environmental Science*; Elsevier: Amsterdam, The Netherlands, 1986; Volume 28, pp. 179–192.
4. Kokabi, M.; Yousefzadi, M. Checklist of the marine macroalgae of Iran. *Bot. Mar.* **2015**, *58*, 307–320. [CrossRef]
5. Sparks, C. *Fundamentals of Marine Riser Mechanics: Basic Principles and Simplified Analyses*; PennWell Books, LLC: Tulsa, OK, USA, 2018.
6. Williamson, C.H.; Govardhan, R. Vortex-induced vibrations. *Annu. Rev. Fluid Mech.* **2004**, *36*, 413–455. [CrossRef]
7. Sarpkaya, T. A critical review of the intrinsic nature of vortex-induced vibrations. *J. Fluids Struct.* **2004**, *19*, 389–447. [CrossRef]
8. Gabbai, R.D.; Benaroya, H. An overview of modeling and experiments of vortex-induced vibration of circular cylinders. *J. Sound Vibr.* **2005**, *282*, 575–616. [CrossRef]
9. DNV. Riser fatigue. In *Recommended Practice DNV-RP-F204*; DNV: Hovik, Norway, 2005.
10. Zeinoddini, M.; Bakhtiari, A.; Ehteshami, M.; Seif, M.S. Towards an understanding of the marine fouling effects on VIV of circular cylinders: Response of cylinders with regular pyramidal roughness. *Appl. Ocean Res.* **2016**, *59*, 378–394. [CrossRef]
11. Jadidi, P.; Zeinoddini, M.; Soltanpour, M.; Zandi, A.P.; Seif, M.S. Towards an understanding of marine fouling effects on VIV of circular cylinders: Aggregation effects. *Ocean Eng.* **2018**, *147*, 227–242. [CrossRef]
12. Bakhtiari, A.; Zeinoddini, M.; Ashrafipour, H.; Tamimi, V.; Harandi, M.A.; Jadidi, P. The effects of marine fouling on the wake-induced vibration of tandem circular cylinders. *Ocean Eng.* **2020**, *216*, 108093. [CrossRef]
13. Zhao, H.; Yin, Y.; Gao, P.; Tian, R.; Li, X.; Tan, S. Numerical studies on the effect of surface roughness on flow field and flow-induced vibration in the in-line tube bundle. *Nucl. Eng. Des.* **2024**, *424*, 113313. [CrossRef]
14. Marty, A.; Berhault, C.; Damblans, G.; Facq, J.V.; Gaurier, B.; Germain, G.; Soulard, T.; Schoefs, F. Experimental study of hard marine growth effect on the hydrodynamical behaviour of a submarine cable. *Appl. Ocean Res.* **2021**, *114*, 102810. [CrossRef]
15. Zou, P.X.; Ruiter, N.; Uijttewaal, W.S.J.; Chen, X.X.; Peters, D.J.; Bricker, J.D. Experimental study of surface roughness effects on hydrodynamic characteristics of a submerged floating tunnel. *Appl. Ocean Res.* **2023**, *135*, 103557. [CrossRef]
16. Ashrafipour, H.; Zeinoddini, M.; Tamimi, V.; Rashki, M.R.; Jadidi, P. Two-degrees-of-freedom vortex-induced vibration of cylinders covered with hard marine fouling. *Int. J. Mech. Sci.* **2022**, *233*, 107624. [CrossRef]
17. Jadidi, P.; Zeinoddini, M. Influence of hard marine fouling on energy harvesting from Vortex-Induced Vibrations of a single-cylinder. *Renew. Energy* **2020**, *152*, 516–528. [CrossRef]
18. Rashki, M.R.; Hejazi, K.; Tamimi, V.; Zeinoddini, M.; Ashrafipour, H. Impacts of hard marine growth on 2DoF VIV-based piezoelectric energy harvesting. *Renew. Energy* **2024**, *231*, 120913. [CrossRef]
19. Huang, J.; Chen, G.; Shu, L.; Chen, Y.; Zhang, Y. Impact of fouling on flow-induced vibration characteristics in fluid-conveying pipelines. *IEEE Access* **2016**, *4*, 6631–6644. [CrossRef]
20. Warby, C.; Dias, F.; Schoefs, F.; Pakrashi, V. An ecologically aware modification of the Morison's equation for long term marine growth effects. *Mech. Res. Commun.* **2024**, *139*, 104293. [CrossRef]
21. Xie, W.; Jiang, Z.; Zheng, Y.; Liang, Z. Dynamic behaviour of a large flexible net with local biofouling subjected to irregular waves. *Biosyst. Eng.* **2025**, *254*, 104138. [CrossRef]
22. Zhu, H.; Li, Y.; Hao, H.; Alam, M.M.; Zhou, T.; Tang, T. Experimental investigation on the vortex-induced vibration of a circular cylinder partially covered with moss. *Ocean Eng.* **2024**, *298*, 117198. [CrossRef]
23. Rashki, M.R.; Hejazi, K.; Tamimi, V.; Zeinoddini, M.; Bagherpour, P.; Harandi, M.A. Electromagnetic energy harvesting from 2DOF-VIV of circular oscillators: Impacts of soft marine fouling. *Energy* **2023**, *282*, 128964. [CrossRef]
24. Rashki, M.R.; Hejazi, K.; Tamimi, V.; Zeinoddini, M.; Harandi, M.A. Impacts of soft marine fouling on the hydrokinetic energy harvesting from one-degree-of-freedom vortex-induced vibrations. *Sust. Energy Technol. Assess.* **2022**, *54*, 102881. [CrossRef]
25. Nobakht-Kolur, F.; Zeinoddini, M.; Harandi, M.A.; Abi, F.A.; Jadidi, P. Effects of soft marine fouling on wave-induced forces in floating aquaculture cages: Physical model testing under regular waves. *Ocean Eng.* **2021**, *238*, 109759. [CrossRef]
26. Nobakht-Kolur, F.; Zeinoddini, M.; Ghalebi, A. Hydrodynamic forces in marine-fouled floating aquaculture cages: Physical modelling under irregular waves. *J. Fluids Struct.* **2021**, *105*, 103331. [CrossRef]
27. Dorogi, D.; Baranyi, L.; Konstantinidis, E. Modulation and hysteresis in vortex-induced vibration of a spring-mounted cylinder in a slowly varying oscillatory stream. *J. Fluids Struct.* **2023**, *122*, 103982. [CrossRef]
28. Zhu, H.; Xu, H.; Liu, B.; Zhong, J. Numerical investigation of the vortex-induced vibration of a circular cylinder in oscillatory flow. *Ocean Eng.* **2024**, *310*, 118666. [CrossRef]
29. Zhang, M.; Fu, S.; Ren, H.; Xu, Y.; Qin, X. Experimental investigation on vortex-induced force of a flexible pipe under oscillatory flow. *Appl. Ocean Res.* **2022**, *126*, 103269. [CrossRef]

30. Deng, D.; Zhao, W.; Wan, D. Numerical study of vortex-induced vibration of a flexible cylinder with large aspect ratios in oscillatory flows. *Ocean Eng.* **2021**, *238*, 109730. [CrossRef]
31. Li, J.; Chen, N.Z. Vortex-Induced Vibration (VIV) of flexible riser conveying severe slugging and straight flow in steady and oscillatory flows. *J. Sound Vib.* **2025**, *595*, 118728. [CrossRef]
32. Xu, A.; Chai, Y.; Li, F.; Chen, Y. Nonlinear vortex-induced vibrations of slightly curved pipes conveying fluid in steady and oscillatory flows. *Ocean Eng.* **2023**, *270*, 113623. [CrossRef]
33. Theophanatos, A. Marine Growth and the Hydrodynamic Loading of Offshore Structures. Ph.D. Thesis, University of Strathclyde, Glasgow, UK, 1988.
34. Theophanatos, A.; Wolfram, J. Hydrodynamic loading on macro-roughened cylinders of various aspect ratios. *J. Offshore Mech. Arct. Eng.* **1989**, *111*, 214–222. [CrossRef]
35. Skaugset, K.; Baarholm, R. Effect of marine growth on an elastically mounted circular cylinder. In Proceedings of the International Conference on Offshore Mechanics and Arctic Engineering, Estoril, Portugal, 15–20 June 2008; Volume 48227, pp. 855–861.
36. Zhou, B.; Wang, X.; Gho, W.M.; Tan, S.K. Force and flow characteristics of a circular cylinder with uniform surface roughness at subcritical Reynolds numbers. *Appl. Ocean Res.* **2015**, *49*, 20–26. [CrossRef]
37. Annapeh, H.F.; Kurushina, V. Flow-Induced Vibrations of a Square Cylinder in the Combined Steady and Oscillatory Flow. *J. Mar. Sci. Eng.* **2025**, *13*, 1621. [CrossRef]
38. Menter, F.R. 2-equation eddy-viscosity turbulence models for engineering applications. *AIAA J.* **1994**, *32*, 1598–1605. [CrossRef]
39. Elmiligui, A.; Abdol-Hamid, K.; Massey, S.; Pao, S. Numerical study of flow past a circular cylinder using RANS, Hybrid RANS/LES and PANS formulations. In Proceedings of the 22nd Applied aerodynamics conference and exhibit, Providence, Rhode Island, 16–19 August 2004; p. 4959.
40. Annapeh, H.F.; Kurushina, V.; Franzini, G.R. Flow-Induced Vibrations of Five Cylinders in Uniform Current. *Vibration* **2025**, *8*, 31. [CrossRef]
41. Postnikov, A.; Pavlovskaia, E.; Wiercigroch, M. 2DOF CFD calibrated wake oscillator model to investigate vortex-induced vibrations. *Int. J. Mech. Sci.* **2017**, *127*, 176–190. [CrossRef]
42. Han, Z.; Zhou, D.; Malla, A.; Nepali, R.; Kushwaha, V.; Li, Z.; Kwok, K.C.; Tu, J.; Bao, Y. Wake-induced vibration interference between a fixed square cylinder and a 2-DOF downstream square cylinder at low Reynolds numbers. *Ocean Eng.* **2018**, *164*, 698–711. [CrossRef]
43. Li, Z.; Yao, W.; Yang, K.; Jaiman, R.K.; Khoo, B.C. On the vortex-induced oscillations of a freely vibrating cylinder in the vicinity of a stationary plane wall. *J. Fluids Struct.* **2016**, *65*, 495–526. [CrossRef]
44. Xu, W.; Wu, H.; Jia, K.; Wang, E. Numerical investigation into the effect of spacing on the flow-induced vibrations of two tandem circular cylinders at subcritical Reynolds numbers. *Ocean Eng.* **2021**, *236*, 109521. [CrossRef]
45. Munir, A.; Zhao, M.; Wu, H.; Ning, D.; Lu, L. Numerical investigation of the effect of plane boundary on two-degree-of-freedom of vortex-induced vibration of a circular cylinder in oscillatory flow. *Ocean Eng.* **2018**, *148*, 17–32. [CrossRef]
46. Okajima, A.; Nagamori, T.; Matsunaga, F.E.; Kiwata, T. Some experiments on flow-induced vibration of a circular cylinder with surface roughness. *J. Fluids Struct.* **1999**, *13*, 853–864. [CrossRef]
47. Jauvtis, N.A.; Williamson, C.H.K. The effect of two degrees of freedom on vortex-induced vibration at low mass and damping. *J. Fluid Mech.* **2004**, *509*, 23–62. [CrossRef]
48. Zhao, M.; Kaja, K.; Xiang, Y.; Yan, G. Vortex-induced vibration (VIV) of a circular cylinder in combined steady and oscillatory flow. *Ocean Eng.* **2013**, *73*, 83–95. [CrossRef]
49. Jusoh, I.; Wolfram, J. Effects of marine growth and hydrodynamic loading on offshore structures. *J. Mek.* **1996**, *1*, 77–98.
50. Zhao, M.; Cheng, L.; An, H. Numerical investigation of vortex-induced vibration of a circular cylinder in transverse direction in oscillatory flow. *Ocean Eng.* **2012**, *41*, 39–52. [CrossRef]
51. Kozakiewicz, A.; Sumer, B.M.; Fredsøe, J.; Hansen, E.A. Vortex regimes around a freely vibrating cylinder in oscillatory flow. *Int. J. Offshore Polar Eng.* **1997**, *7*, 94–103.
52. Sumer, B.M.; Fredsøe, J. Transverse vibrations of an elastically mounted cylinder exposed to an oscillating flow. *J. Offshore Mech. Arct. Eng.* **1988**, *110*, 387–394. [CrossRef]